NANO LETTERS

pubs.acs.org/NanoLett

Letter

Vibrational Properties in Highly Strained Hexagonal Boron Nitride Bubbles

Elena Blundo, Alessandro Surrente, Davide Spirito, Giorgio Pettinari, Tanju Yildirim, Carlos Alvarado Chavarin, Leonetta Baldassarre, Marco Felici, and Antonio Polimeni*

Cite This: https://doi.org/10.1021/acs.nanolett.1c04197

Read Online

ACCESS | Metrics & More | Article Recommendations | Supporting Information

ABSTRACT: Hexagonal boron nitride (hBN) is widely used as a protective layer for few-atom-thick crystals and heterostructures (HSs), and it hosts quantum emitters working up to room temperature. In both instances, strain is expected to play an important role, either as an unavoidable presence in the HS fabrication or as a tool to tune the quantum emitter electronic properties. Addressing the role of strain and exploiting its tuning potentiality require the development of efficient methods to control it and of reliable tools to quantify it. Here we present a technique based on hydrogen irradiation to induce the formation of wrinkles and bubbles in hBN, resulting in remarkably high strains of ∼2%. By combining infrared (IR) near-field scanning optical microscopy and micro-Raman measurements with numerical calculations, we characterize the response to strain for both IR-active and Raman-active modes, revealing the potential of the vibrational properties of hBN as highly sensitive strain probes.

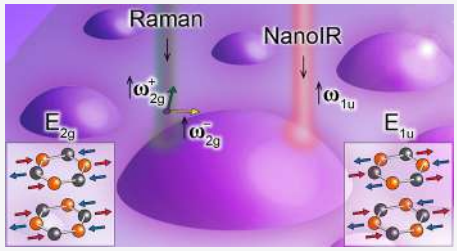

KEYWORDS: *strain, hBN, 2D materials, Raman, nano-IR, phonons*

I. INTRODUCTION

Hexagonal boron nitride (hBN), a wide-gap layered material,[1] features a marked chemical inertness[2,3] and mechanical robustness.[4] Thanks to these properties, hBN is an ideal substrate or capping material for two-dimensional crystals,[5−10] protecting them from oxidation[11] and bringing about a substantial improvement of the charge-carrier mobility and of the light emission characteristics.[7,8,12] Indeed, hBN capping is routinely employed to fabricate high-quality heterostructures (HSs), wherein intriguing carrier potential landscapes can be realized.[13,14] The fabrication process relies on mechanical stacking, often leading to the emergence of strain in the different layers and to important modifications of their electronic states.[15] hBN is also attracting increasing interest for its intrinsic properties, sustaining the propagation of hyperbolic phonon-polaritons (HPPs)[16,17] and hosting single-photon emitters operating at room temperature.[18−22] Its remarkable mechanical robustness (breaking strengths of ∼70 GPa and Young's modulus of ∼800 GPa[4,23,24]) was exploited for high-quality mechanical resonators[25] and to reversibly tune the emission wavelength of single-photon emitters via stretching.[26] Strained wrinkles were also found to be ideal candidates for launching HPPs.[27] It follows that in hBN, like in other two-dimensional materials, strain plays a relevant role.[24] Different methods were employed to induce strain in thin layers of hBN, for example, by deposition on substrates subject to stretching,[26] bending,[28] or thermal compression[29] or by nanoindentation.[4] Great attention was also attracted by the formation of hBN bubbles ensuing gas trapping,[30] hydrogen-plasma exposure,[31] or pressure-induced bulging.[23] Such bubbles may be the ultimate platforms for probing the elastic/adhesive properties of two-dimensional materials, owing to the strong interplay between these properties and the bubble morphology.[23,32−34] Although hBN bubbles are expected to host sizable strains, as theoretically predicted and experimentally confirmed in similar graphene[35] and transition-metal dichalcogenide (TMD) structures,[33,36−40] where total strains of 1−5% were achieved, no clear evidence of strain has been provided so far. More generally, the effect of strain on the vibrational properties of thin hBN has surprisingly not received systematic attention, with only a few Raman studies published to date, focusing on the moderate strain regime (<0.4%).[28,29,41]

Here we report on a method to mechanically deform hBN based on the low-energy hydrogen (H) or deuterium (D) ion irradiation of multilayer flakes. Depending on the flake thickness, H/D-ion treatments lead to the formation of nano/micrometric bubbles or wrinkles. Unlike methods based on the deposition of ultrathin films,[30] the proposed technique permits the formation of wrinkles and bubbles with a high density and on flakes with virtually unrestricted size. In

Received: October 31, 2021
Revised: January 25, 2022

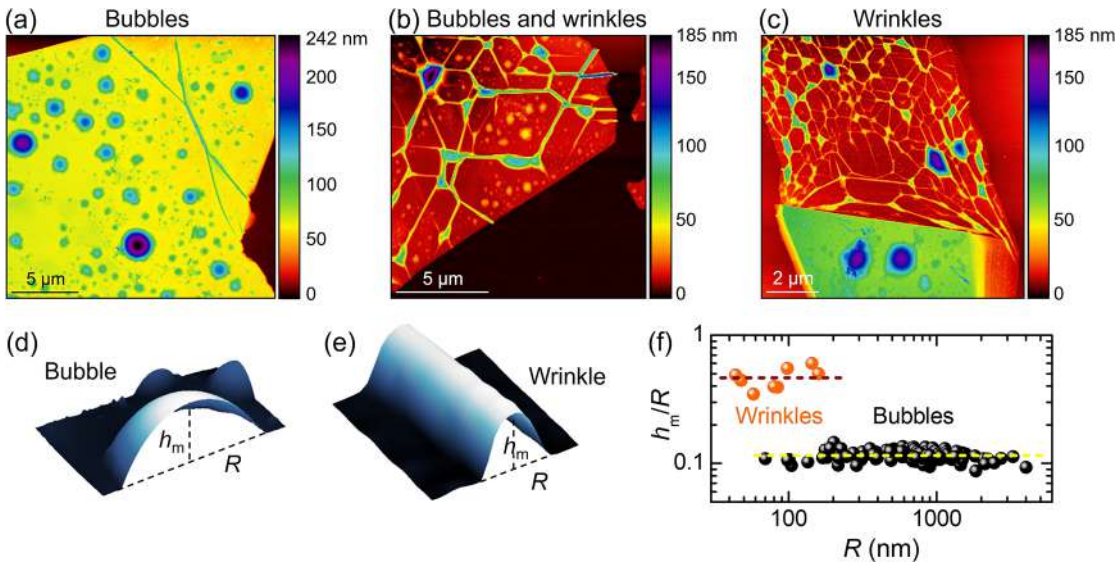

Figure 1. Formation of hydrogen-filled bubbles and of wrinkles in hBN. (a−c) AFM images of multilayer hBN flakes after H irradiation. The flakes have thicknesses of (a) 55, (b) 10, and (c) 5 nm (thin part corresponding to the top side of the figure), and the images show the presence of only bubbles, both bubbles and wrinkles, and only wrinkles, respectively. (d,e) 3D AFM images of half a bubble (panel d, where R = 2.06 μm and h_m = 225 nm) and part of a wrinkle (panel e, where R = 144 nm and h_m = 88 nm). The definitions of maximum height (h_m) and footprint radius (R) are depicted. (f) Statistical analysis of the aspect ratios (h_m/R) measured in wrinkles and bubbles. The dashed lines represent the average aspect ratios estimated for each set of data.

addition, we can control the thickness of the bubbles from a few layers to tens of layers by tuning the energy or changing the isotope of the ion beam. We employed an infrared (IR) scanning near-field optical microscope (SNOM) to perform nanoscale Fourier transform IR (nano-FTIR) measurements and an optical microscope to perform micro-Raman (μ-Raman) measurements. Across the bubble surfaces, we observe record large shifts of both the IR-active and Raman-active modes in excess of 50 cm^{-1}. With the support of numerical modeling of the strain distribution, we extract the Grüneisen parameters of hBN and, by performing linearly polarized Raman spectroscopy, its shear deformation potential.

II. RESULTS AND DISCUSSION

We exfoliated thick hBN flakes from commercial hBN crystals (HQ graphene). The flakes were deposited on Si/SiO_2 substrates and initially characterized by atomic force microscopy (AFM); see the Supporting Information, Methods. The samples were subjected to H (or D)-ion irradiation by a Kaufman ion gun[37,42] under high vacuum conditions at 150 °C, with the samples electrically grounded to avoid charging. For details, see the Supporting Information, Methods. To avoid the formation of defects, we employed low ion-beam energies of <35 eV. After the treatment, optical microscope images of the flakes may reveal a slightly nonhomogeneous coloration related to the presence of barely visible circular or elongated features; see Supporting Figure S1. AFM measurements demonstrate the presence of bubbles, wrinkles, or both on the flakes, as shown in Figure 1a−c and Supporting Figure S2. A statistical AFM study (see Supporting Figure S3) allows us to establish a correspondence between the different morphologies and the flake thickness t: For $t \gtrsim 10$ nm, only bubbles form (Figure 1a); for $t \simeq 10$ nm, both bubbles and wrinkles can be observed (Figure 1b); and in thin flakes with $t \lesssim 10$ nm, wrinkles and irregular structures predominate (Figure 1c). In the latter case, molecular hydrogen likely forms, accumulates, and percolates at the flake/substrate interface, giving rise to irregular structures and wrinkles (Figure 1c); see also Supporting Figure S3. On the contrary, the formation of spherically shaped bubbles in thick flakes ($t \gtrsim 10$ nm) can be attributed to the formation and trapping of molecular hydrogen in the hBN interlayers, as observed in H-plasma-treated hBN,[31] and in TMDs.[37] We thus hypothesize that protons with kinetic energies of ∼10−30 eV penetrate through hBN for ∼10 nm and that the formation of wrinkles or bubbles depends on where H_2 remains caged. To support this hypothesis, we intentionally induced the explosion of some bubbles via a high-power (some milliwatts), highly focused laser beam and measured the height difference between the crater of the exploded bubble and the flake surface outside the crater by AFM. In samples irradiated with H ions (beam energies <34 eV) (see Supporting Figure S4), we measured thicknesses ranging from 1.8 to 12 nm (corresponding to about 5 to 36 monolayers). To form thinner bubbles, instead, we irradiated some samples with deuterium ions (beam energies <25 eV), which are known to penetrate less through hBN with respect to protons,[43] and we measured bubble thicknesses as thin as ∼0.5 nm (i.e., a couple of layers); see Supporting Figure S4. This demonstrates the remarkable flexibility of our method, which, unlike H-plasma-based methods,[31] enables us to obtain bubbles thinner than 10 monolayers. The long durability of the bubbles and Raman studies of the irradiated flakes (see Supporting Figure S5) suggest that the low-energy beams employed here do not induce a sizable amount of defects in the crystal, unlike higher energy heavier atom beams.[44−50]

We performed AFM measurements to study the morphological properties of bubbles and wrinkles and measured their aspect ratio h_m/R, where h_m is the maximum height of the object and R is its half width. (See Figure 1d,e). The results are summarized in Figure 1f. The wrinkles feature a narrow width distribution and aspect ratios in the 0.3 to 0.6 range. The bubbles show a much wider size distribution and a size-

https://doi.org/10.1021/acs.nanolett.1c04197
Nano Lett. XXXX, XXX, XXX−XXX

independent aspect ratio, as expected based on previous theoretical[30,32,51] and experimental[30−32,37,38,52] studies. For our bubbles, we find $h_m/R = 0.115 \pm 0.011$, in agreement with that reported for hydrocarbon-filled monolayer bubbles[30] and multilayer bubbles created by H-plasma treatments.[31] The constant aspect ratio, independent of size and thickness, testifies that the mechanics of the bubbles is dominated by stretching, whereas the bending contribution is negligible,[32,53] at variance with other kinds of bent, yet not pressurized, systems.[54] Importantly, the strain scales as $(h_m/R)^2$;[32] therefore, a similar strain distribution is expected independent of the bubble formation method and thickness. Next, we address such distribution on hBN bubbles.

One of the most common means for evaluating the amount of strain in two-dimensional materials is provided by a quantitative analysis of the frequency of the lattice vibration normal modes.[24] Typically, lattice stretching (i.e., tensile strain) induces a softening of the phonon modes. Furthermore, under anisotropic strains, the double-degenerate in-plane modes split as a result of the lowered crystal symmetry. The shift rate and splitting rate of the vibrational modes can thus be conveniently used to assess the strain magnitude and its anisotropy degree in atomically thin membranes.[24] This is especially important when the actual strain differs from the expected strain, like in many bending or stretching devices,[24] or cannot be estimated theoretically. In this work, we focus on two specific in-plane transverse modes, which are IR-active (E_{1u}) and Raman-active (E_{2g}). Their lattice displacements are sketched in Figure 2.

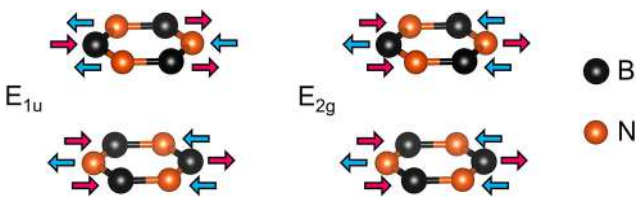

Figure 2. Sketch of the atom displacements corresponding to the IR-active E_{1u} mode and to the Raman-active E_{2g} mode. Differently colored arrows indicate opposite atom motions.

Figure 3a displays the AFM image of a circular hBN bubble with diameter $D = 2R = 4.54\ \mu$m and height $h_m = 267$ nm ($h_m/R = 0.117$) obtained by D irradiation. The AFM profile recorded along the cyan dashed line is shown in Figure 3b (circles). The yellow line is the profile evaluated by finite element method (FEM) numerical calculations; see the Supporting Information, Methods. The latter also provides the strain distribution,[32,37] as shown on the left side of Figure 3c, where ε_r and ε_θ are the radial and circumferential in-plane strain components in polar coordinates, respectively.[32,53] The calculated spatial distribution of the total strain $\varepsilon_{tot} = \varepsilon_r + \varepsilon_\theta$ is displayed as a false-color image on the right side of panel c. Strain features an anisotropic character, changing from tensile uniaxial at its edge ($r/R = 1$, $\varepsilon_r \neq 0$ and $\varepsilon_\theta = 0$) to tensile equi-biaxial at the summit of the bubble ($r/R = 0$, $\varepsilon_r = \varepsilon_\theta$). On these premises, we expect the in-plane transverse phonon frequency ω_t to undergo a decrease with respect to unstrained hBN due to stretching, as well as a splitting in ω_t^+ and ω_t^-, the extent of which depends on the position on the bubble. Thus we introduce the average frequency

$$\omega_t^{av} = \frac{\omega_t^+ + \omega_t^-}{2} \tag{1}$$

and mode splitting

$$\sigma_t = \omega_t^+ - \omega_t^- \tag{2}$$

The frequency variation upon strain can be quantified by the shift rate

$$\Delta = -\frac{\partial \omega_t^{av}}{\partial \varepsilon_{tot}} \tag{3}$$

and splitting rate

$$\Sigma = \frac{\partial \sigma_t}{\partial \varepsilon_{diff}} \tag{4}$$

where $\varepsilon_{tot}(r) = \varepsilon_r(r) + \varepsilon_\theta(r)$ and $\varepsilon_{diff}(r) = \varepsilon_r(r) - \varepsilon_\theta(r)$.

Equivalently, one can introduce dimensionless quantities, such as the Grüneisen parameter

$$\gamma = \frac{\Delta}{\omega_t^0} \tag{5}$$

and the shear deformation potential

$$\beta = \frac{\Sigma}{\omega_t^0} \tag{6}$$

where ω_t^0 is the mode frequency in the absence of strain.

The E_{1u} mode (see lattice displacements in Figure 2) was studied by nano-FTIR SNOM measurements;[55,56] see the Supporting Information, Methods. This technique has been widely employed in two-dimensional systems, for example, to probe phonon-polaritons in hBN,[27,57,58] phonons in hBN superlattices,[59] electron−phonon interactions in graphene,[60] and intersubband transitions in two-dimensional quantum wells,[61] but the E_{1u} hBN mode sensitivity to strain has not been investigated, to our knowledge. Figure 3d shows the normalized near-field amplitude $S(\omega,r)$, as obtained with a spectral line scan along the gray short dashed line in Figure 3a. The near-field signal originates from the tip−sample interaction and provides a lateral resolution of ∼20 nm; see the Supporting Information, Methods. The corresponding spectra are shown in Figure 3e. The phonon peak frequency from the bulk region outside the bubble is $\omega_{1u} = 1367$ cm^{-1}, in agreement with previous reports.[62] An abrupt decrease in ω_{1u} is noticed when the tip approaches the bubble's edge, where a 0.9% tensile strain is already present. (See Figure 3c.) On moving further toward the bubble center, ω_{1u} seamlessly decreases, in agreement with the expected tensile strain increase. To quantify the mode shift variation versus the total strain $\varepsilon_{tot}(r)$, we established a one-to-one correspondence between the AFM-derived bubble profile (h vs r) and the calculated strain components shown in Figure 3c. In turn, this allowed us to establish a correspondence between each measured ω_{1u} and $\varepsilon_{tot}(r)$, given that the $h(r)$ values were measured by the SNOM tip at the very same points where ω_{1u} was probed. To reduce the background signal, we collected the near-field data at several harmonics. In Figure 3f, we show the spatial dependence of the second and third harmonics of the signal associated with the E_{1u} phonon. (See the Supporting Information, Methods and Supporting Note 1.) We reproduce quite successfully the dependence of ω_{1u} on r using as fitting parameters the mode frequency at zero strain $\omega_{1u}^0 = (1369.7 \pm$

https://doi.org/10.1021/acs.nanolett.1c04197
Nano Lett. XXXX, XXX, XXX−XXX

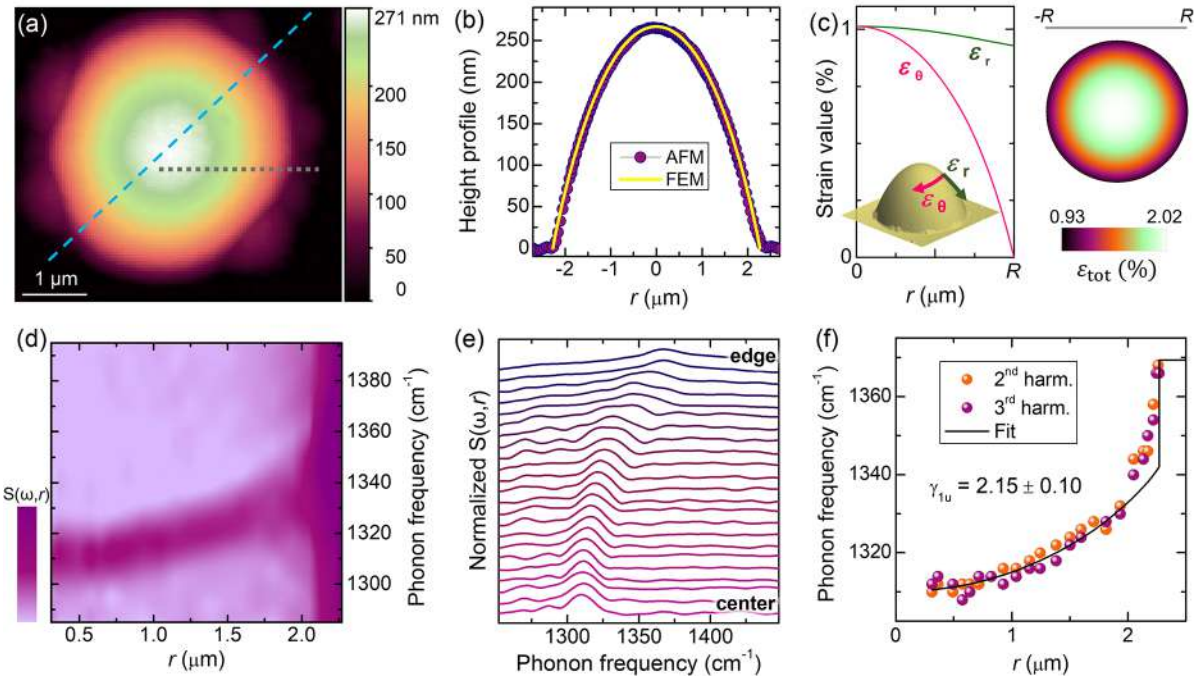

Figure 3. IR-active mode versus strain. (a) 2D AFM image of a hBN bubble exhibiting a circular symmetric shape but on its edge, where smaller satellite bubbles nucleated. The bubble has $R = 2.27$ μm and $h_m = 267$ nm ($h_m/R = 0.117$) and was created in a deuterated sample (beam energy equal to 6 eV) to minimize the bubble thickness. (b) Comparison between the AFM profile acquired along a diameter of the bubble (highlighted in panel a by a cyan dashed line) and the profile obtained by FEM calculations. (c) Left: Radial dependence, obtained by FEM calculations, of the in-plane circumferential (ε_θ) and radial (ε_r) strain components, a sketch of which is depicted as the inset. Right: Spatial distribution of the total in-plane strain $\varepsilon_{tot} = \varepsilon_r + \varepsilon_\theta$. (d,e) Color map of the near-field amplitude $S(\omega,r)$ (d) and corresponding spectra (e), where the IR-active mode (E_{1u}) is visible. The measurements were taken along the gray short dashed line shown in panel a. The second harmonic is considered here. (f) IR phonon frequency dependence on the radial distance r, as deduced from the spectra shown in panel e and the AFM profile. The third-harmonic data are also included here. The black solid line is a fit to the data assuming a linear dependence of the phonon frequency on ε_{tot}, provided by eqs 3 and 5.

Table 1. Effect of Strain on the Vibrational Modes[a]

mode	ω_t^0 (cm^{-1})	Δ (cm^{-1}/%)	γ_t	Σ_t (cm^{-1}/%)	β_t	β_t/γ_t
E_{1u} (IR)	1369.9 ± 2.3	29.4 ± 1.8	2.15 ± 0.12			
	1369.7 ± 2.4	29.5 ± 1.4	2.15 ± 0.10			
	1369.0 ± 5.2	36.2 ± 3.6	2.64 ± 0.27			
E_{2g} (Raman)	1370[b]	24.6 ± 0.60	1.79 ± 0.04	11.2 ± 1.9	0.82 ± 0.14	0.46 ± 0.08
	1370[b]	25.1 ± 4.5	1.83 ± 0.33			
	1370[b]	28.5 ± 8.4	2.08 ± 0.61	15.6 ± 3.8	1.14 ± 0.28	0.56 ± 0.14
	1370[b]	33.2 ± 5.2	2.43 ± 0.40			

[a]Parameters obtained for the E_{1u} and E_{2g} from the nano-FTIR and Raman measurements, respectively, The frequency at zero strain (ω_t), shift rate (Δ), Grüneisen parameter (γ_t), splitting rate (Σ_t), shear deformation potential (β_t), and ratio γ_t/β_t were estimated for several bubbles. [b]This value was kept fixed because it was otherwise affected by too large uncertainties.

2.4) cm^{-1} and the shift rate $\Delta_{1u} = (29.5 \pm 1.4)$ cm^{-1}/%, resulting in a Grüneisen parameter (see eq 5) $\gamma_{1u} = 2.15 \pm 0.10$. Analogous measurements were performed on other bubbles; see Supporting Note 1 and Table 1.

It should be noticed that the zero-strain limit ω_{1u}^0 (~1370 cm^{-1}) of the bubble E_{1u} mode is larger than that of bulk hBN (~1367 cm^{-1}). This is consistent with the frequency increase reported for the Raman-active E_{2g} mode in the few-layer limit.[29,63,64]

Let us now discuss our studies of the E_{2g} mode. (See the lattice displacements in Figure 2.) We performed μ-Raman measurements of the hBN bubble ($R = 1.61$ μm, $h_m = 179$ nm, $h_m/R = 0.111$, created by D irradiation), whose AFM image is shown as the inset of Figure 4c. Figure 4a is the spectrally and spatially resolved intensity map of the light scattered by the bubble in the spectral region of the E_{2g} mode. The map was recorded along a diameter (see the inset of panel c), and the corresponding spectra are shown in Figure 4b. The spot size and spectral resolution are ~0.5 μm and 0.7 cm^{-1}, respectively; see the Supporting Information, Methods. The intense peak at 1366.2 cm^{-1} comes from the bulk hBN flake from which the bubble swelled. The E_{2g} signal from the bubble is much less intense due to the reduced thickness and exhibits a spatially dependent and lower frequency due to strain. We notice that unlike the IR signal, the Raman signal becomes negligibly small as the laser approaches the edge of the bubble due to optical interference effects.[37,39] The correspondence between the measured ω_{2g} values and $\varepsilon_{tot}(r) = \varepsilon_r(r) + \varepsilon_\theta(r)$ is established by evaluating the strain via FEM calculations based on the AFM profile; see Supporting Figure S6. The spatial dependence of ω_{2g} is shown in Figure 4c, and it is best reproduced with a shift rate $\Delta_{2g} = (28.5 \pm 8.4)$ cm^{-1}/% and a Grüneisen

https://doi.org/10.1021/acs.nanolett.1c04197
Nano Lett. XXXX, XXX, XXX−XXX

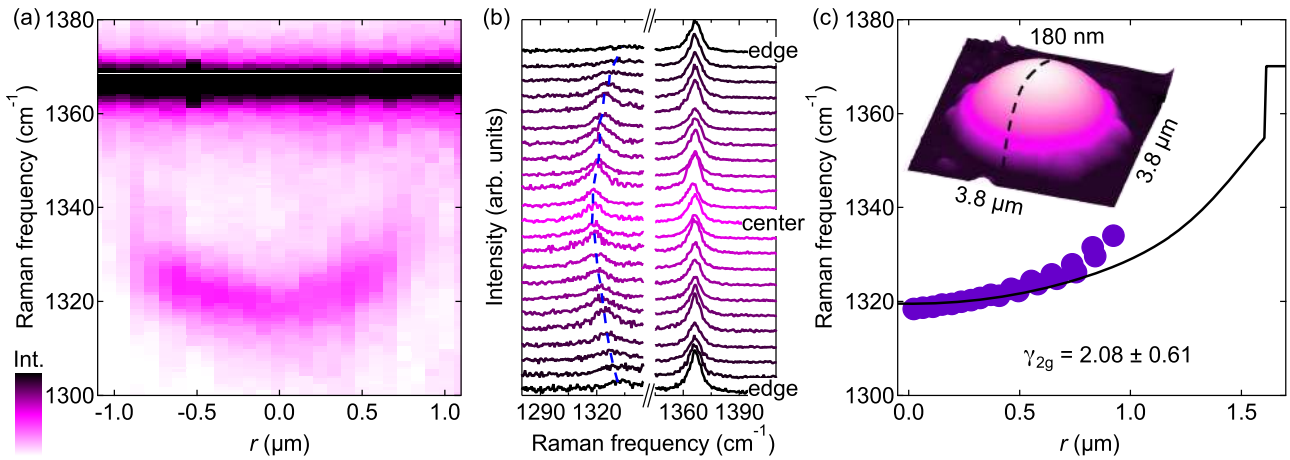

Figure 4. Raman-active mode versus strain. (a) False-color image of the intensity of the E_{2g} Raman mode as a function of the position along a diameter of a bubble. The bubble has R = 1.61 μm and h_m = 179 nm (h_m/R = 0.111) and was created in a deuterated sample (beam energy equal to 25 eV). (b) Raman spectra corresponding to the map of panel a. (c) E_{2g} Raman-mode frequencies as a function of the distance from the center of the bubble. The solid line is a linear fit to the frequency versus r behavior, with γ_{2g} being the fitting parameter. Inset: AFM image of the investigated structure. The dashed line indicates the diameter along which the spectra were measured.

parameter (see eq 5) γ_{2g} = 2.08 ± 0.61. The extrapolation frequency at zero strain was set at 1370 cm^{-1}, which is greater than the corresponding bulk mode (1366.2 cm^{-1}), like in the case of the E_{1u} IR-active mode and consistent with published results.[29,63,64] Similar measurements performed on different bubbles are shown in Supporting Note 2, and the estimated parameters are displayed in Table 1. We also performed a statistical analysis of the shift at the bubble summit including many other bubbles, giving average Grüneisen parameters γ_{2g} = 2.04 ± 0.48 (Δ_{2g} = (27.9 ± 6.6) cm^{-1}/%); see Supporting Note 3. Our statistical analysis also shows how E_{1u} and E_{2g} are characterized by similar Grüneisen parameters.

Previous μ-Raman studies on hBN bubbles created by H-plasma treatments[31] reported only a modest shift of ∼3 cm^{-1} between the bubble center and the bulk hBN. Similar small shifts (∼3 cm^{-1}) were observed in hBN monolayers subject to thermal compression (biaxial strain of −0.17%),[29] resulting in γ_{2g} = 0.62. Finally, uniaxial strains of up to 0.4% were applied to thin hBN flakes (two to four layers) using a bending apparatus, achieving frequency softenings of <6 cm^{-1}. Grüneisen parameters γ_{2g} between 1.77 and 2.07 were estimated in this case[28] and were, on average, slightly lower than our estimates. (See Table 1.) By comparison with the current literature, our approach permits us to achieve a much larger total strain, on average, equal to ∼1.9%, with unprecedented shifts in excess of 50 cm^{-1}.

In addition to the E_{2g} mode shift, a splitting is expected in the bubbles due to the imbalance between ε_θ and ε_r; see Supporting Figure S6. Figure 5a displays an intensity map formed by polarization-dependent μ-Raman spectra recorded on a given point of the same bubble of Figure 4. The point is 790 nm away from the center (i.e., r/R = 0.49) and is marked by a black dot superimposed on the strain anisotropy degree plot in Figure 5c, with the anisotropy being defined as $\alpha = (\varepsilon_r - \varepsilon_\theta)/(\varepsilon_r + \varepsilon_\theta)$. Therein, the arrows indicate the strain direction. The radial distance r was determined by the relationship between ω_{2g} and r given in Figure 4c. Each spectrum of Figure 5a was recorded by keeping the polarization direction of the laser fixed at an arbitrary, unknown angle ϕ_0 with respect to a reference crystal direction (e.g., the armchair/zigzag direction). Likewise, strain is oriented along the bubble radius, and its direction is thus also fixed at an unknown angle θ with respect to the same lattice reference. The angle ϕ between the polarization of the Raman-scattered and Raman-exciting photons was then varied from 0 to 360°. Whereas the E_{2g} bulk mode at 1366.2 cm^{-1} remains constant in intensity and frequency, the strain-softened E_{2g} mode of the bubble in the 1320−1340 cm^{-1} range exhibits a marked angular dependence of its center-of-mass frequency, pointing to a mode splitting. This is exemplified in Figure 5b, showing two μ-Raman spectra recorded with opposite polarizations (ϕ = 0 and 90°). Indeed, it can be demonstrated that the intensities $I^{\pm}_{2g}$ of the $E^{\pm}_{2g}$ modes split by uniaxial strain are given by[24]

$$I^{+}_{2g} = c^2 \cos^2(\phi + 2\phi_0 + \theta)$$

$$I^{-}_{2g} = c^2 \sin^2(\phi + 2\phi_0 + \theta)$$

$$I_{2g} = I^{+}_{2g} + I^{-}_{2g} = c^2 \quad (7)$$

where c is a constant. By performing a line-shape fitting of the Raman spectra (see Supporting Note 4), we extracted $I^{\pm}_{2g}$ as a function of ϕ, where E^{+}_{2g} and E^{-}_{2g} refer to the high- and low-frequency components, respectively. Figure 5d shows the resulting polar plot obtained from the data of panel a. The reference angle ($2\phi_0 + \theta$) is set to zero for simplicity reasons. The two components are clearly in counter phase, as expected. Figure 5e shows a similar set of measurements acquired on a point of the bubble positioned symmetrically at 90° with respect to the previous one (at r = 680 nm); see the gray dot in panel c. In this case, the strain direction is given by $\theta' = \theta$ + 90°, and as a consequence of eq 7, the $E^{\pm}_{2g}$ components follow an angular dependence that is $\pi/2$ out-of-phase with respect to that of the previous point (Figure 5d). These results are fully consistent with the strain field calculated numerically, whereby the ε_r component dictates the strain direction. Finally, the μ-Raman spectra recorded at the bubble center (white dot in panel c), where the strain is equi-biaxial, show no mode splitting; see Figure 5f. Other polarization maps were acquired in different points of the bubble. For each point, the average frequency ω^{av}_{2g} corresponds to a given r value. (See Figure 4c.) In turn, via numerical simulations (see Supporting Figure S6),

https://doi.org/10.1021/acs.nanolett.1c04197
Nano Lett. XXXX, XXX, XXX−XXX

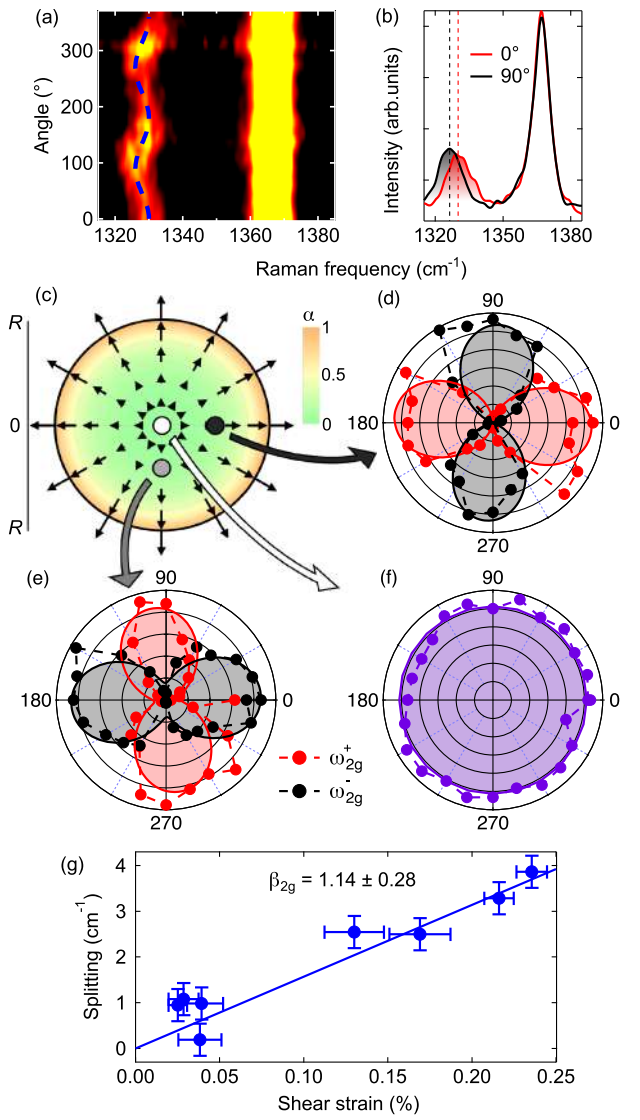

Figure 5. (a) False-color map of the intensity of the E_{2g} Raman mode as a function of the angle of the polarization analyzer. The dashed line is a sinusoidal guide to the eye. (b) μ-Raman spectra measured with polarizations parallel and perpendicular to the uniaxial strain direction. (c) Radial dependence of the strain anisotropy $\alpha = (\varepsilon_r - \varepsilon_\theta)/(\varepsilon_r + \varepsilon_\theta)$, based on FEM calculations. The arrows point to the direction of the strain field. Their length is calculated as $\log_{10}(100\alpha)$. The dots depict the position of the excitation spots of the polarization-resolved Raman measurements. (d−f) Intensity of the low-frequency (ω^-_{1u}) and high-frequency (ω^+_{1u}) Raman modes as a function of the analyzer angle for excitation performed (d) on the right (black dot), (e) at the bottom (gray dot), and (f) at the center of a bubble (white dot). (g) Mode splitting as a function of the shear strain. The solid line is a linear fit.

we obtain $\varepsilon_{shear}(r) = \varepsilon_{diff}(r) = \varepsilon_r(r) - \varepsilon_\theta(r)$. Figure 5g shows the dependence of the mode splitting σ_{2g} versus $\varepsilon_{shear}(r)$. Considering eq 6, we estimate a splitting rate $\Sigma_{2g} = 15.6 \pm 3.8$ $cm^{-1}/\%$ and a shear deformation potential $\beta_{2g} = 1.14 \pm 0.28$. Thus for this bubble, we get $\beta_{2g}/\gamma_{2g} = 0.56 \pm 0.14$. We performed similar measurements on another bubble with a lower Grüneisen parameter (see Supporting Note 4) and found $\beta_{2g} = 0.82 \pm 0.14$ and $\beta_{2g}/\gamma_{2g} = 0.46 \pm 0.08$ (see Table 1), showing how the ratio β_{2g}/γ_{2g} is less affected by fluctuations than β_{2g} and γ_{2g}. We are aware of only one previous report of the hBN shear potential in the few-layer limit, where the ratio β_{2g}/γ_{2g} was found to vary between 0.45 and 0.52.[28]

III. CONCLUSIONS

We irradiated bulk hBN flakes with low-energy hydrogen or deuterium ions. The ions penetrate through the crystal for a few nanometers, and molecular hydrogen or deuterium forms, inducing the blistering of a few atomic planes and hence the formation of micro/nano-metric wrinkles or bubbles. Wrinkles or bubbles predominate for flake thicknesses of $t \lesssim 10$ nm or $\gtrsim 10$ nm, respectively. The bubbles were investigated in detail because they exhibit tensile strains with a remarkably high ~2% maximum value, exceeding that typically achieved for hBN in bending/stretching devices.[28,29,41] The effects of strain on the IR-active (E_{1u}) and Raman-active (E_{2g}) in-plane modes were studied over the bubble surface by spatially resolved nano-FTIR and polarization-dependent μ-Raman, respectively. The large amount of strain and its anisotropic character toward the edge of the bubbles permitted to derive shift and splitting rates on the order of 30 and 15 $cm^{-1}/\%$, respectively. These values are comparable to those reported in graphene and are about one order of magnitude larger than those found in TMDs, InSe, and black phosphorus.[24] These findings show that the vibrational properties of hBN are extremely sensitive probes of mechanical deformations, and thus they can be exploited to assess the stress status of two-dimensional HSs and hBN-based quantum emitters.

■ ASSOCIATED CONTENT

Supporting Information

The Supporting Information is available free of charge at https://pubs.acs.org/doi/10.1021/acs.nanolett.1c04197.

Methods section and notes on IR-SNOM and Raman mapping or statistical measurements and of polarization-resolved Raman measurements in hBN bubbles, additional optical and AFM images of hBN bubbles and wrinkles, and additional FEM calculations (PDF)

■ AUTHOR INFORMATION

Corresponding Author

Antonio Polimeni − *Physics Department, Sapienza University of Rome, 00185 Rome, Italy;* orcid.org/0000-0002-2017-4265; Email: antonio.polimeni@uniroma1.it

Authors

Elena Blundo − *Physics Department, Sapienza University of Rome, 00185 Rome, Italy;* orcid.org/0000-0003-0423-4798

Alessandro Surrente − *Physics Department, Sapienza University of Rome, 00185 Rome, Italy; Department of Experimental Physics, Faculty of Fundamental Problems of Technology, Wroclaw University of Science and Technology, Wroclaw 50-370, Poland;* orcid.org/0000-0003-4078-4965

Davide Spirito − *IHP-Leibniz Institut fur Innovative Mikroelektronik, 15236 Frankfurt (Oder), Germany;* orcid.org/0000-0002-6074-957X

Giorgio Pettinari − *Institute for Photonics and Nanotechnologies (CNR-IFN), National Research Council, 00156 Rome, Italy*

https://doi.org/10.1021/acs.nanolett.1c04197
Nano Lett. XXXX, XXX, XXX−XXX

Tanju Yildirim − *Center for Functional Sensor & Actuator (CFSN), National Institute for Materials Science (NIMS), Tsukuba, Ibaraki 305-0044, Japan*
Carlos Alvarado Chavarin − *IHP-Leibniz Institut fur Innovative Mikroelektronik, 15236 Frankfurt (Oder), Germany*
Leonetta Baldassarre − *Physics Department, Sapienza University of Rome, 00185 Rome, Italy; IHP-Leibniz Institut fur Innovative Mikroelektronik, 15236 Frankfurt (Oder), Germany*
Marco Felici − *Physics Department, Sapienza University of Rome, 00185 Rome, Italy*

Complete contact information is available at:
https://pubs.acs.org/10.1021/acs.nanolett.1c04197

Notes

The authors declare no competing financial interest.

■ ACKNOWLEDGMENTS

We thank Emmanuele Cappelluti and Habib Rostami for useful discussions and Yuerui Lu for previous work in the field. A.P. and M.F. acknowledge support by Sapienza Università di Roma under grants "Ricerche Ateneo" 2018 and 2019 and "Progetti H2020-Collaborativi". E.B., A.P., and M.F. acknowledge funding from the Regione Lazio programme "Progetti di Gruppi di ricerca" legge Regionale n. 13/2008 (SINFONIA project, prot. n. 85-2017-15200) via LazioInnova spa. A.S. gratefully acknowledges funding from the European Union's Horizon 2020 research and innovation programme under the Marie Skłodowska-Curie grant agreement no. 844837. L.B. acknowledges support from the PRIN2017 grant number 2017Z8TS5B and from the IHP Microelectronics "Wolfgang Mehr" Fellowship Award.

■ REFERENCES

(1) Watanabe, K.; Taniguchi, T.; Kanda, H. Direct-bandgap properties and evidence for ultraviolet lasing of hexagonal boron nitride single crystal. *Nat. Mater.* **2004**, *3*, 404−409.
(2) Liu, Z.; Gong, Y.; Zhou, W.; Ma, L.; Yu, J.; Idrobo, J. C.; Jung, J.; MacDonald, A. H.; Vajtai, R.; Lou, J.; Ajayan, P. M. Ultrathin high-temperature oxidation-resistant coatings of hexagonal boron nitride. *Nat. Commun.* **2013**, *4*, 2541.
(3) Li, L. H.; Cervenka, J.; Watanabe, K.; Taniguchi, T.; Chen, Y. Strong oxidation resistance of atomically thin boron nitride nanosheets. *ACS Nano* **2014**, *8*, 1457−1462.
(4) Falin, A.; Cai, Q.; Santos, E. J.; Scullion, D.; Qian, D.; Zhang, R.; Yang, Z.; Huang, S.; Watanabe, K.; Taniguchi, T.; Barnett, M. R.; Chen, Y.; Ruoff, R. S.; Li, L. H. Mechanical properties of atomically thin boron nitride and the role of interlayer interactions. *Nat. Commun.* **2017**, *8*, 15815.
(5) Raja, A.; Waldecker, L.; Zipfel, J.; Cho, Y.; Brem, S.; Ziegler, J. D.; Kulig, M.; Taniguchi, T.; Watanabe, K.; Malic, E.; et al. Dielectric disorder in two-dimensional materials. *Nat. Nanotechnol.* **2019**, *14*, 832−837.
(6) Dean, C. R.; Young, A. F.; Meric, I.; Lee, C.; Wang, L.; Sorgenfrei, S.; Watanabe, K.; Taniguchi, T.; Kim, P.; Shepard, K. L.; Hone, J. Boron nitride substrates for high-quality graphene electronics. *Nat. Nanotechnol.* **2010**, *5*, 722−726.
(7) Cadiz, F.; Courtade, E.; Robert, C.; Wang, G.; Shen, Y.; Cai, H.; Taniguchi, T.; Watanabe, K.; Carrere, H.; Lagarde, D.; Manca, M.; Amand, T.; Renucci, P.; Tongay, S.; Marie, X.; Urbaszek, B. Excitonic linewidth approaching the homogeneous limit in MoS_2-based van der Waals heterostructures. *Phys. Rev. X* **2017**, *7*, No. 021026.
(8) Ajayi, O. A; Ardelean, J. V; Shepard, G. D; Wang, J.; Antony, A.; Taniguchi, T.; Watanabe, K.; Heinz, T. F; Strauf, S.; Zhu, X-Y; Hone, J. C Approaching the intrinsic photoluminescence linewidth in transition metal dichalcogenide monolayers. *2D Mater.* **2017**, *4*, No. 031011.
(9) Chen, X.; Wu, Y.; Wu, Z.; Han, Y.; Xu, S.; Wang, L.; Ye, W.; Han, T.; He, Y.; Cai, Y.; Wang, N. High-quality sandwiched black phosphorus heterostructure and its quantum oscillations. *Nat. Commun.* **2015**, *6*, 7315.
(10) Mayorov, A. S.; Gorbachev, R. V.; Morozov, S. V.; Britnell, L.; Jalil, R.; Ponomarenko, L. A.; Blake, P.; Novoselov, K. S.; Watanabe, K.; Taniguchi, T.; Geim, A. K. Micrometer-scale ballistic transport in encapsulated graphene at room temperature. *Nano Lett.* **2011**, *11*, 2396−2399.
(11) Arora, H.; Jung, Y.; Venanzi, T.; Watanabe, K.; Taniguchi, T.; Hübner, R.; Schneider, H.; Helm, M.; Hone, J. C.; Erbe, A. Effective Hexagonal Boron Nitride Passivation of Few-Layered InSe and GaSe to Enhance Their Electronic and Optical Properties. *ACS Appl. Mater. Interfaces* **2019**, *11*, 43480.
(12) Wierzbowski, J.; Klein, J.; Sigger, F.; Straubinger, C.; Kremser, M.; Taniguchi, T.; Watanabe, K.; Wurstbauer, U.; Holleitner, A. W.; Kaniber, M.; Müller, K.; Finley, J. J. Direct exciton emission from atomically thin transition metal dichalcogenide heterostructures near the lifetime limit. *Sci. Rep.* **2017**, *7*, 12383.
(13) Tartakovskii, A. Excitons in 2D heterostructures. *Nat. Rev. Phys.* **2020**, *2*, 8−9.
(14) Tartakovskii, A. Moiré or not. *Nat. Mater.* **2020**, *19*, 581−582.
(15) Bai, Y.; Zhou, L.; Wang, J.; Wu, W.; McGilly, L. J.; Halbertal, D.; Lo, C. F. L.; Liu, F.; Ardelean, J.; Rivera, P.; Finney, N. R.; Yang, X.-C.; Basov, D. N.; Yao, W.; Xu, X.; Hone, J.; Pasupathy, A. N.; Zhu, X.-Y. Excitons in strain-induced one-dimensional moiré potentials at transition metal dichalcogenide heterojunctions. *Nat. Mater.* **2020**, *19*, 1068−1073.
(16) Dai, S.; Fei, Z.; Ma, Q.; Rodin, A. S.; Wagner, M.; McLeod, A. S.; Liu, M. K.; Gannett, W.; Regan, W.; Watanabe, K.; Taniguchi, T.; Thiemens, M.; Dominguez, G.; Neto, A. H. C.; Zettl, A.; Keilmann, F.; Jarillo-Herrero, P.; Fogler, M. M.; Basov, D. N. Tunable phonon polaritons in atomically thin van der Waals crystals of boron nitride. *Science* **2014**, *343*, 1125−1129.
(17) Caldwell, J. D.; Kretinin, A. V.; Chen, Y.; Giannini, V.; Fogler, M. M.; Francescato, Y.; Ellis, C. T.; Tischler, J. G.; Woods, C. R.; Giles, A. J.; Hong, M.; Watanabe, K.; Taniguchi, T.; Maier, S. A.; Novoselov, K. S. Sub-diffractional volume-confined polaritons in the natural hyperbolic material hexagonal boron nitride. *Nat. Commun.* **2014**, *5*, 5221.
(18) Tran, T. T.; Bray, K.; Ford, M. J.; Toth, M.; Aharonovich, I. Quantum emission from hexagonal boron nitride monolayers. *Nat. Nanotechnol.* **2016**, *11*, 37−41.
(19) Tran, T. T.; Elbadawi, C.; Totonjian, D.; Lobo, C. J.; Grosso, G.; Moon, H.; Englund, D. R.; Ford, M. J.; Aharonovich, I.; Toth, M. Robust multicolor single photon emission from point defects in hexagonal boron nitride. *ACS Nano* **2016**, *10*, 7331−7338.
(20) Bourrellier, R.; Meuret, S.; Tararan, A.; Stéphan, O.; Kociak, M.; Tizei, L. H.; Zobelli, A. Bright UV single photon emission at point defects in h-BN. *Nano Lett.* **2016**, *16*, 4317−4321.
(21) Vogl, T.; Lu, Y.; Koy Lam, P. Room temperature single photon source using fiber-integrated hexagonal boron nitride. *J. Phys. D: Appl. Phys.* **2017**, *50*, 295101.
(22) Fournier, C.; Plaud, A.; Roux, S.; Pierret, A.; Rosticher, M.; Watanabe, K. W.; Taniguchi, T.; Buil, S.; Qulin, X.; Barjon, J.; Hermier, J.-P.; Delteil, H. Position-controlled quantum emitters with reproducible emission wavelength in hexagonal boron nitride. *Nat. Commun.* **2021**, *12*, 3779.
(23) Wang, G.; Dai, Z.; Xiao, J.; Feng, S.; Weng, C.; Liu, L.; Xu, Z.; Huang, R.; Zhang, Z. Bending of multilayer van der Waals materials. *Phys. Rev. Lett.* **2019**, *123*, 116101.
(24) Blundo, E.; Cappelluti, E.; Felici, M.; Pettinari, G.; Polimeni, A. Strain-tuning of the electronic, optical, and vibrational properties of two-dimensional crystals. *Appl. Phys. Rev.* **2021**, *8*, No. 021318.
(25) Shandilya, P. K.; Fröch, J. E.; Mitchell, M.; Lake, D. P.; Kim, S.; Toth, M.; Behera, B.; Healey, C.; Aharonovich, I.; Barclay, P. E.

Hexagonal boron nitride cavity optomechanics. *Nano Lett.* **2019**, *19*, 1343−1350.
(26) Mendelson, N.; Doherty, M.; Toth, M.; Aharonovich, I.; Tran, T. T. Strain-Induced Modification of the Optical Characteristics of Quantum Emitters in Hexagonal Boron Nitride. *Adv. Mater.* **2020**, *32*, 1908316.
(27) Duan, J.; Chen, R.; Li, J.; Jin, K.; Sun, Z.; Chen, J. Launching phonon polaritons by natural boron nitride wrinkles with modifiable dispersion by dielectric environments. *Adv. Mater.* **2017**, *29*, 1702494.
(28) Androulidakis, C.; Koukaras, E.; Poss, M.; Papagelis, K.; Galiotis, C.; Tawfick, S. Strained hexagonal boron nitride: Phonon shift and Grüneisen parameter. *Phys. Rev. B* **2018**, *97*, 241414.
(29) Cai, Q.; Scullion, D.; Falin, A.; Watanabe, K.; Taniguchi, T.; Chen, Y.; Santos, E. J.; Li, L. H. Raman signature and phonon dispersion of atomically thin boron nitride. *Nanoscale* **2017**, *9*, 3059−3067.
(30) Khestanova, E.; Guinea, F.; Fumagalli, L.; Geim, A.; Grigorieva, I. Universal shape and pressure inside bubbles appearing in van der Waals heterostructures. *Nat. Commun.* **2016**, *7*, 12587.
(31) He, L.; Wang, H.; Chen, L.; Wang, X.; Xie, H.; Jiang, C.; Li, C.; Elibol, K.; Meyer, J.; Watanabe, K.; Taniguchi, T.; Wu, Z.; Wang, W.; Ni, Z.; Miao, X.; Zhang, C.; Zhang, D.; Wang, H.; Xie, X. Isolating hydrogen in hexagonal boron nitride bubbles by a plasma treatment. *Nat. Commun.* **2019**, *10*, 2815.
(32) Blundo, E.; Yildirim, T.; Pettinari, G.; Polimeni, A. Experimental Adhesion Energy in van der Waals Crystals and Heterostructures from Atomically Thin Bubbles. *Phys. Rev. Lett.* **2021**, *127*, No. 046101.
(33) Di Giorgio, C.; Blundo, E.; Pettinari, G.; Felici, M.; Lu, Y.; Cucolo, A. M.; Polimeni, A.; Bobba, F. Nanoscale Measurements of Elastic Properties and Hydrostatic Pressure in H_2-Bulged MoS_2 Membranes. *Adv. Mater. Interfaces* **2020**, *7*, 2001024.
(34) Di Giorgio, C.; Blundo, E.; Pettinari, G.; Felici, M.; Polimeni, A.; Bobba, F. Exceptional Elasticity of Microscale Constrained MoS_2 Domes. *ACS Appl. Mater. Interfaces* **2021**, *13*, 48228.
(35) Zabel, J.; Nair, R. R.; Ott, A.; Georgiou, T.; Geim, A. K.; Novoselov, K. S.; Casiraghi, C. Raman spectroscopy of graphene and bilayer under biaxial strain: bubbles and balloons. *Nano Lett.* **2012**, *12*, 617−621.
(36) Lloyd, D.; Liu, X.; Christopher, J. W.; Cantley, L.; Wadehra, A.; Kim, B. L.; Goldberg, B. B.; Swan, A. K.; Bunch, J. S. Band gap engineering with ultralarge biaxial strains in suspended monolayer MoS_2. *Nano Lett.* **2016**, *16*, 5836−5841.
(37) Tedeschi, D.; Blundo, E.; Felici, M.; Pettinari, G.; Liu, B.; Yildrim, T.; Petroni, E.; Zhang, C.; Zhu, Y.; Sennato, S.; Lu, Y.; Polimeni, A. Controlled Micro/Nanodome Formation in Proton-Irradiated Bulk Transition-Metal Dichalcogenides. *Adv. Mater.* **2019**, *31*, 1903795.
(38) Blundo, E.; Di Giorgio, C.; Pettinari, G.; Yildirim, T.; Felici, M.; Lu, Y.; Bobba, F.; Polimeni, A. Engineered creation of periodic giant, non-uniform strains in MoS_2 monolayers. *Adv. Mater. Interfaces* **2020**, *7*, 2000621.
(39) Blundo, E.; Felici, M.; Yildirim, T.; Pettinari, G.; Tedeschi, D.; Miriametro, A.; Liu, B.; Ma, W.; Lu, Y.; Polimeni, A. Evidence of the direct-to-indirect band gap transition in strained two-dimensional WS_2, MoS_2, and WSe_2. *Phys. Rev. Res.* **2020**, *2*, No. 012024.
(40) Tyurnina, A. V.; Bandurin, D. A.; Khestanova, E.; Kravets, V. G.; Koperski, M.; Guinea, F.; Grigorenko, A. N.; Geim, A. K.; Grigorieva, I. V. Strained bubbles in van der Waals heterostructures as local emitters of photoluminescence with adjustable wavelength. *ACS Photonics* **2019**, *6*, 516−524.
(41) Androulidakis, C.; Galiotis, C. Thermomechanical behaviour of hexagonal boron nitride at elevated temperatures. *2D Mater.* **2020**, *7*, No. 045011.
(42) Felton, J.; Blundo, E.; Ling, S.; Glover, J.; Kudrynskyi, Z. R.; Makarovsky, O.; Kovalyuk, Z. D.; Besley, E.; Walker, G.; Polimeni, A.; Patanè, A. The Interaction of Hydrogen with the van der Waals Crystal γ-InSe. *Molecules* **2020**, *25*, 2526.
(43) Lozada-Hidalgo, M.; Hu, S.; Marshall, O.; Mishchenko, A.; Grigorenko, A.; Dryfe, R.; Radha, B.; Grigorieva, I.; Geim, A. Sieving hydrogen isotopes through two-dimensional crystals. *Science* **2016**, *351*, 68−70.
(44) Chejanovsky, N.; Rezai, M.; Paolucci, F.; Kim, Y.; Rendler, T.; Rouabeh, W.; Fávaro de Oliveira, F.; Herlinger, P.; Denisenko, A.; Yang, S.; Gerhardt, I.; Finkler, A.; Smet, J. H.; Wrachtrup, J. Structural Attributes and Photodynamics of Visible Spectrum Quantum Emitters in Hexagonal Boron Nitride. *Nano Lett.* **2016**, *16*, 7037−7045.
(45) Choi, S.; Tran, T. T.; Elbadawi, C.; Lobo, C.; Wang, X.; Juodkazis, S.; Seniutinas, G.; Toth, M.; Aharonovich, I. Engineering and Localization of Quantum Emitters in Large Hexagonal Boron Nitride Layers. *ACS Appl. Mater. Interfaces* **2016**, *8*, 29642−29648.
(46) Ziegler, J.; Klaiss, R.; Blaikie, A.; Miller, D.; Horowitz, V. R.; Alemán, B. J. Deterministic Quantum Emitter Formation in Hexagonal Boron Nitride via Controlled Edge Creation. *Nano Lett.* **2019**, *19*, 2121−2127.
(47) Gu, R.; Wang, L.; Zhu, H.; Han, S.; Bai, Y.; Zhang, X.; Li, B.; Qin, C.; Liu, J.; Guo, G.; Shan, X.; Xiong, G.; Gao, J.; He, C.; Han, Z.; Liu, X.; Zhao, F. Engineering and Microscopic Mechanism of Quantum Emitters Induced by Heavy Ions in hBN. *ACS Photonics* **2021**, *8*, 2912−2922.
(48) Fischer, M.; Caridad, J. M.; Sajid, A.; Ghaderzadeh, S.; Ghorbani-Asl, M.; Gammelgaard, L.; Bøggild, P.; Thygesen, K. S.; Krasheninnikov, A. V.; Xiao, S.; Wubs, M.; Stenger, N. Controlled generation of luminescent centers in hexagonal boron nitride by irradiation engineering. *Sci. Adv.* **2021**, *7*, No. eabe7138.
(49) Mendelson, N.; Chugh, D.; Reimers, J. R.; Cheng, T. S.; Gottscholl, A.; Long, H.; Mellor, C. J.; Zettl, A.; Dyakonov, V.; Beton, P. H.; Novikov, S. V.; Jagadish, C.; Tan, H. H.; Ford, M. J.; Toth, M.; Bradac, C.; Aharonovich, I. Identifying carbon as the source of visible single-photon emission from hexagonal boron nitride. *Nat. Mater.* **2021**, *20*, 321−328.
(50) Zhang, H.; Lan, M.; Tang, G.; Chen, F.; Shu, Z.; Chen, F.; Li, M. Discrete color centers in two-dimensional hexagonal boron nitride induced by fast neutron irradiation. *J. Mater. Chem. C* **2019**, *7*, 12211−12216.
(51) Aslyamov, T.; Iakovlev, E.; Akhatov, I. S.; Zhilyaev, P. Model of graphene nanobubble: Combining classical density functional and elasticity theories. *J. Chem. Phys.* **2020**, *152*, No. 054705.
(52) Jia, Z.; Dong, J.; Liu, L.; Nie, A.; Xiang, J.; Wang, B.; Wen, F.; Mu, C.; Zhao, Z.; Xu, B.; Gong, Y.; Tian, Y.; Liu, Z. Photoluminescence and Raman Spectra Oscillations Induced by Laser Interference in Annealing-Created Monolayer WS_2 Bubbles. *Adv. Opt. Mater.* **2019**, *7*, 1801373.
(53) Wang, P.; Gao, W.; Cao, Z.; Liechti, K. M.; Huang, R. Numerical analysis of circular graphene bubble. *J. Appl. Mech.* **2013**, *80*, No. 040905.
(54) Han, E.; Yu, J.; Annevelink, E.; Son, J.; Kang, D. A.; Watanabe, K.; Taniguchi, T.; Ertekin, E.; Huang, P. Y.; van der Zande, A. M. Ultrasoft slip-mediated bending in few-layer graphene. *Nat. Mater.* **2020**, *19*, 305.
(55) Huth, F.; Govyadinov, A.; Amarie, S.; Nuansing, W.; Keilmann, F.; Hillenbrand, R. Nano-FTIR absorption spectroscopy of molecular fingerprints at 20 nm spatial resolution. *Nano Lett.* **2012**, *12*, 3973−3978.
(56) Mastel, S.; Govyadinov, A. A.; de Oliveira, T. V.; Amenabar, I.; Hillenbrand, R. Nanoscale-resolved chemical identification of thin organic films using infrared near-field spectroscopy and standard Fourier transform infrared references. *Appl. Phys. Lett.* **2015**, *106*, No. 023113.
(57) Shi, Z.; Bechtel, H. A.; Berweger, S.; Sun, Y.; Zeng, B.; Jin, C.; Chang, H.; Martin, M. C.; Raschke, M. B.; Wang, F. Amplitude- and phase-resolved nanospectral imaging of phonon polaritons in hexagonal boron nitride. *ACS Photonics* **2015**, *2*, 790−796.
(58) Li, P.; Lewin, M.; Kretinin, A. V.; Caldwell, J. D.; Novoselov, K. S.; Taniguchi, T.; Watanabe, K.; Gaussmann, F.; Taubner, T. Hyperbolic phonon-polaritons in boron nitride for near-field optical imaging and focusing. *Nat. Commun.* **2015**, *6*, 7507.

https://doi.org/10.1021/acs.nanolett.1c04197
Nano Lett. XXXX, XXX, XXX−XXX

(59) Moore, S. L.; Ciccarino, C. J.; Halbertal, D.; McGilly, L. J.; Finney, N. R.; Yao, K.; Shao, Y.; Ni, G.; Sternbach, A.; Telford, E. J.; Kim, B. S.; Rossi, S. E.; Watanabe, K.; Taniguchi, T.; Pasupathy, A. N.; Dean, C. R.; Hone, J.; Schuck, P. J.; Narang, P.; Basov, D. N. Nanoscale lattice dynamics in hexagonal boron nitride moiré superlattices. *Nat. Commun.* **2021**, *12*, 5741.

(60) Qian, J.; Luan, Y.; Kim, M.; Ho, K.-M.; Shi, Y.; Wang, C.-Z.; Li, Y.; Fei, Z. Nonequilibrium phonon tuning and mapping in few-layer graphene with infrared nanoscopy. *Phys. Rev. B* **2021**, *103*, L201407.

(61) Schmidt, P.; Vialla, F.; Latini, S.; Massicotte, M.; Tielrooij, K.-J.; Mastel, S.; Navickaite, G.; Danovich, M.; Ruiz-Tijerina, D. A.; Yelgel, C.; Fal'ko, V.; Thygesen, K. S.; Hillenbrand, R.; Koppens, F. H. L. Nano-imaging of intersubband transitions in van der Waals quantum wells. *Nat. Nanotechnol.* **2018**, *13*, 1035.

(62) Geick, R.; Perry, C. H.; Rupprecht, G. Normal Modes in Hexagonal Boron Nitride. *Phys. Rev.* **1966**, *146*, 543.

(63) Gorbachev, R. V.; Riaz, I.; Nair, R. R.; Jalil, R.; Britnell, L.; Belle, B. D.; Hill, E. W.; Novoselov, K. S.; Watanabe, K.; Taniguchi, T.; Geim, A. K.; Blake, P. Hunting for Monolayer Boron Nitride: Optical and Raman Signatures. *Small* **2011**, *7*, 465−468.

(64) Krecmarova, M.; Andres-Penares, D.; Fekete, L.; Ashcheulov, P.; Molina-Sánchez, A.; Canet-Albiach, R.; Gregora, I.; Mortet, V.; Martínez-Pastor, J. P.; Sánchez-Royo, J. F. Optical Contrast and Raman Spectroscopy Techniques Applied to Few-Layer 2D Hexagonal Boron Nitride. *Nanomaterials* **2019**, *9*, 1047.

https://doi.org/10.1021/acs.nanolett.1c04197
Nano Lett. XXXX, XXX, XXX−XXX

SUPPORTING INFORMATION for

Vibrational properties in highly strained hexagonal boron nitride bubbles

Elena Blundo,[1] Alessandro Surrente,[1,2] Davide Spirito,[3] Giorgio Pettinari,[4] Tanju Yildirim,[5] Carlos Alvarado Chavarin,[3] Leonetta Baldassarre,[1,3] Marco Felici,[1] and Antonio Polimeni[1,*]

[1] *Physics Department, Sapienza University of Rome, 00185, Roma, Italy.*
[2] *Department of Experimental Physics, Faculty of Fundamental Problems of Technology, Wroclaw University of Science and Technology, Wroclaw 50-370, Poland* [3] *IHP-Leibniz Institut fur Innovative Mikroelektronik, Im Technologiepark 25, 15236 Frankfurt (Oder), Germany*
[4] *Institute for Photonics and Nanotechnologies (CNR-IFN), National Research Council, 00156 Roma, Italy.*
[5] *Center for Functional Sensor and Actuator (CFSN), Research Center for Functional Materials, National Institute for Materials Science (NIMS), 1-1 Namiki, Tsukuba, Ibaraki 305-0044, Japan.*

* Corresponding author: antonio.polimeni@uniroma1.it

Contents

Methods

Sample fabrication and cleaning procedure. hBN flakes were mechanically exfoliated by the scotch tape method and deposited on Si/SiO_2 substrates. AFM measurements were thus performed to check the status of the flake surface before H-ion irradiation. Whenever adhesive tape residuals were found, the samples were cleaned by acetone and IPA baths.

Atomic force microscopy. AFM measurements were performed using a Veeco Digital Instruments Dimension D3100 microscope equipped with a Nanoscope IIIa controller, employing Tapping Mode monolithic silicon probes with a nominal tip curvature radius of $5 - 10\,\mathrm{nm}$ and a force constant of $40\,\mathrm{N\,m^{-1}}$ or metal-coated nano-FTIR tips from NeaSpec. All the scans were performed at room temperature and at ambient conditions. All the data were analysed with the Gwyddion software.

Finite-Element Method calculations. Finite-element method (FEM) calculations using nonlinear-membrane theory were employed to model the profile and strain field of the bubbles [1]. To this end, we employed a model implemented in COMSOL Multiphysics 5.1. Thanks to the mirrored symmetry about the longitudinal axis of the bubbles, an axisymmetric formulation using polar coordinates was used. A line element is used to simulate the membrane with the starting thickness t of a single or several layers of hBN. One end of the line element is subject to a fixed constraint (*i.e.*, null displacement) while the rest of the line is free to move in the longitudinal direction. The presence of a fluid within the bubble is modelled as a pressure load acting on the flat membrane surface, thus causing the bubble inflation. The membrane is deformed until the footprint radius R and the maximum height h_0 reach the target value, which is achieved by varying the internal pressure. The effects of the bending stiffness are neglected since $h_0/t \gg 1.5$ [1]. An extra fine mesh is used for all simulations and a 0.001 convergence setting is used to ensure the numerical accuracy of the solutions. A constant Newtonian solver is used for the numerical solver procedure. Due to the anisotropic stiffness of the layered compounds, an anisotropic stiffness matrix was implemented in the linear elastic material node. The elastic matrix (that relates the stress tensor to the strain tensor) used in this work is [2]:

$$C = \begin{pmatrix} 860.2 & 191.9 & 1.2 & 0 & 0 & 0 \\ 191.9 & 860.2 & 1.2 & 0 & 0 & 0 \\ 1.2 & 1.2 & 5.9 & 0 & 0 & 0 \\ 0 & 0 & 0 & 2.4 & 0 & 0 \\ 0 & 0 & 0 & 0 & 2.4 & 0 \\ 0 & 0 & 0 & 0 & 0 & 334.2 \end{pmatrix}; \tag{0.1}$$

As expected, no differences were observed in the strain components for layer thicknesses from 1 to 20 layers (only very small discrepancies of the order of 10^{-4} were observed).

nano-FTIR measurements. The infrared spectra were collected with a SNOM microscope (NeaSNOM from NeaSpec). A difference-frequency generation laser, yielding a linearly polarized, broadband IR radiation, is focused on a gold-coated AFM probe tip through a parabolic mirror, also used to collect the backscattered radiation. The AFM is operated in tapping mode at $\sim 220\,\mathrm{kHz}$. The scattered signal is demodulated at several higher harmonics n, and, by selecting those with $n \geq 2$, one has a signal dominated by the near-field interaction of the tip with the sample over the far-field scattered background. The SNOM setup is based on an asymmetric Michelson interferometer (the tip and sample are in one of the arms of a Michelson interferometer), which provides both amplitude and phase of the backscattered radiation [3]. The scattered signal is collected by a N_2-cooled MCT (Mercury-Cadmium-Telluride) detector. Measurements were taken by averaging ten interferograms with an $8\,\mathrm{cm^{-1}}$ spectral resolution

[4]. The demodulated phase and amplitude signals are normalized to the reference quantities measured on an Au patches in the vicinity of the flakes of interest as

$$\eta_n(\omega) = s_n^{\mathrm{norm}} \mathrm{e}^{\mathrm{i}\phi_n^{\mathrm{norm}}} = \frac{s_n^{\mathrm{flake}}}{s_n^{\mathrm{ref}}} \mathrm{e}^{\mathrm{i}\left(\phi_n^{\mathrm{flake}} - \phi_n^{\mathrm{ref}}\right)}, \tag{0.2}$$

where s is the near-field amplitude, ϕ the phase, and the suffix n indicates the nth harmonic demodulation. As shown in the literature for materials such as hBN, where one measures strong phonon modes, the scattered amplitude provides the best way to identify the vibrational modes of the flake [5, 6]. It should be noticed that for the SNOM technique, polarization plays a relevant role in many cases, such as the intersubband transitions in two-dimensional heterostructures, where the transition can only be excited by light polarized in the vertical direction [7]. For hBN phonons, however, the SNOM technique allows one to measure both the in-plane and out-of plane transverse optical modes [5, 8].

Raman measurements. For Raman measurements, the excitation laser was provided by a single frequency Nd:YVO_4 lasers (DPSS series by Lasos) emitting at 532 nm, or by a diode laser emitting at 405 nm. The Raman signal was spectrally dispersed by a 750 mm focal length ACTON SP750 monochromator equipped with a 1200 groove/mm grating and detected by a back-illuminated N_2-cooled Si CCD camera (100BRX by Princeton Instruments). The laser light was filtered out by a very sharp long-pass Razor edge filter (Semrock). The micro-Raman (μ-Raman) spectral resolution was $0.7\,\mathrm{cm}^{-1}$. A 100× objective with NA=0.9 was employed to excite and collect the light, in a backscattering configuration. The laser spot size was experimentally determined as follows: The laser was scanned across a reference sample, lithographically patterned with features of known width (1 µm). The intensity of the reflected light was fitted with the ideal reflectance profile, convolved with a Gaussian peak. The standard deviation of this peak, obtained as a fitting parameter, provides our estimate of $\sigma = 0.23 \pm 0.01\,\mu\mathrm{m}$. In establishing the correspondence between strain and radial distance r, a convolution of the strain distribution within the laser spot was duly taken into account.

Supporting Note 1. IR-SNOM mapping measurements in hBN bubbles

Comparison between different harmonics

nanoFTIR spectra are measured with a near-field microscope (sSNOM, NeaSNOM from Nea-SPEC, see Methods). The broadband illumination is focused via a parabolic mirror on the sample and the AFM tip. As the focus is diffraction-limited, there is an unavoidable background that arises from the light scattered by the sample regions that are not under the tip apex and by the tip shaft. In order to suppress the contribution of the background to the total signal, it is possible to demodulate the signal at high harmonics of the tip oscillation frequency, thus obtaining the near-field signal scattered from the volume under the tip only [9]. In Fig. 1.1, we show line scans taken on the bubble of Fig. 3 of the main text, ad specifically along the grey short-dashed line in Fig. 3(a). Supporting Fig. 1.1 compares the signal amplitude $S(\omega, r)$ at different harmonic demodulations. The scattered signal recorded at the fundamental harmonic shows the signature of the phonon peak of the unstrained hBN coming from outside the bubble or from beneath the bubble together with the red-shifted phonon mode of the strained material. Moving to the amplitude demodulated at the second harmonic, we can detect only the signal scattered by the thin strained hBN that comprises the bubble, and an almost identical line scan is obtained at the 3rd harmonic demodulation.

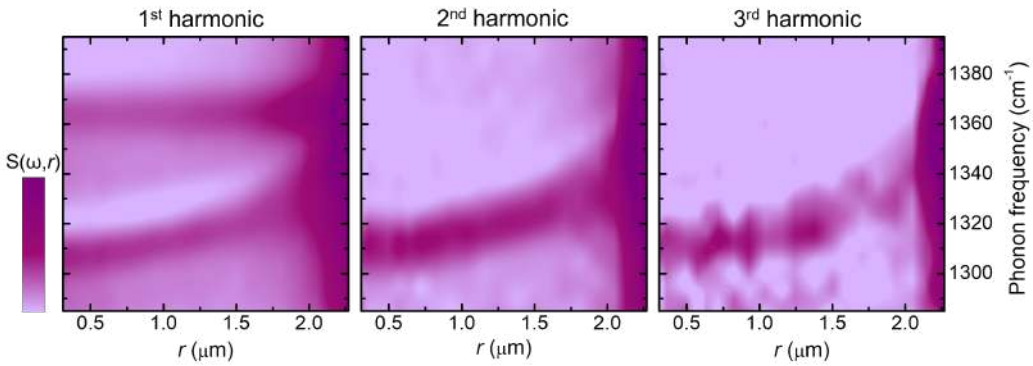

Figure 1.1: Comparison among the first three harmonics of the scattered signal obtained by nanoFTIR line scans taken along the grey short-dashed line in Fig. 3(a) of the main text.

Mapping measurements of other bubbles

To complement the results presented in Fig. 3 of the main text, we performed similar nanoFTIR measurements on other two bubbles. In Fig. 1.2(a), we show the AFM image of the second bubble we studied. This bubble has $R = 0.94$ μm and $h_{\mathrm{m}} = 99$ nm, resulting in $h_{\mathrm{m}}/R = 0.105$. The height profile of this bubble measured along a diameter (cyan dashed line in panel (a)) is shown in panel (b). The nanoFTIR measurements were taken along the same diameter. FEM calculations reproduce quite well the height profile. Indeed, this bubble features a lower aspect ratio with respect to that of Fig. 3 of the main text. This results in a lower strain, whose maximum value reaches 1.5 %, as shown in panel (c). Analogously to the case of the previous bubble, we show the first three harmonics of the scattered amplitude associated to the IR phonon, see panel (d). The measurements were performed along the cyan dashed line superimposed to the AFM image in panel (a). Similarly to the previsou bubble, the 1st harmonic shows the signature of both the strained bubble phonon peak and that of the unstrained hBN outside or

beneath the bubble. In the second harmonic there is still a weak trace of the unstrained hBN, which is instead negligible in the line scan of the third harmonic. By exploiting the one-to-one correspondence between $\varepsilon_{\rm tot} = \varepsilon_r + \varepsilon_\theta$ and r determined in panel (c), we performed a fit to the data in panel (e), providing an extrapolation frequency at null strain $\omega^0_{\rm 1u} = (1369.0 \pm 5.2)$ cm^{-1} and a shift rate $\Delta_{\rm 1u} = (36.2 \pm 3.6)$ cm^{-1}/%, resulting in a Grüneisen parameter (see Equation 5 of the main text) $\gamma_{\rm 1u} = 2.64 \pm 0.27$.

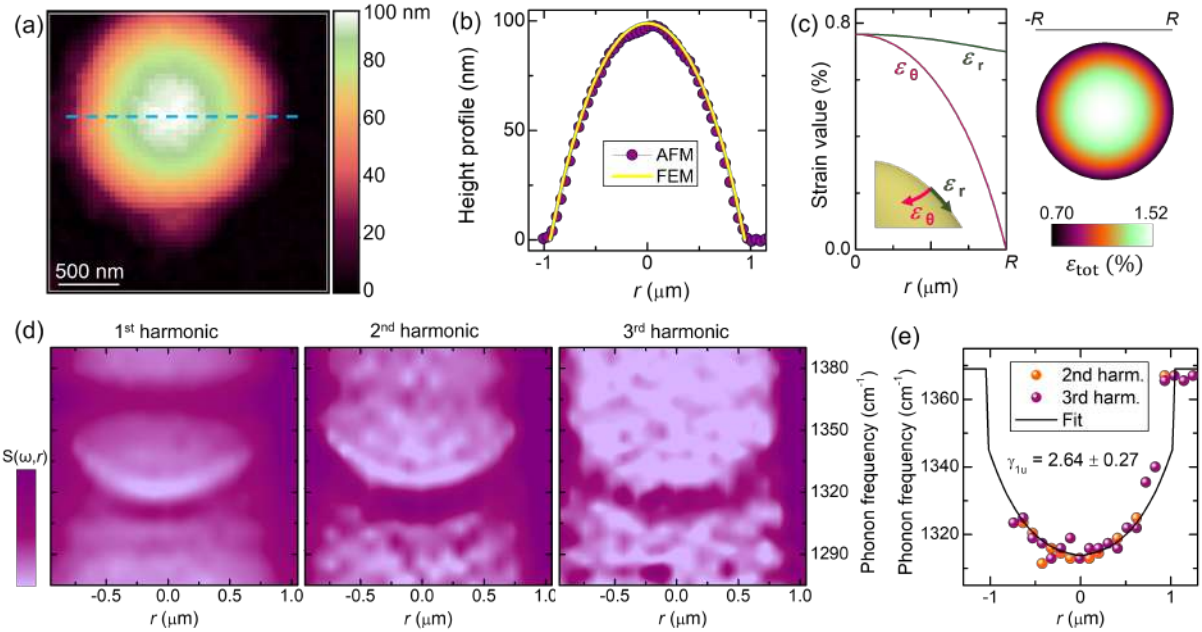

Figure 1.2: IR-active mode *vs* strain for a second bubble. (a) 2D AFM image of a circular hBN bubble, with $R = 0.94$ μm and $h_{\rm m} = 99$ nm ($h_{\rm m}/R = 0.105$) and created in a deuterated sample (beam energy equal to 6 eV). (b) Comparison between the AFM profile acquired along a diameter of the bubble (highlighted in panel (a) by a cyan dashed line) and the profile obtained by FEM calculations. (c) Left: Radial dependence —obtained by FEM calculations— of the in-plane circumferential (ε_θ) and radial (ε_r) strain components, a sketch of which is depicted as inset. Right: Spatial distribution of the total in-plane strain $\varepsilon_{tot} = \varepsilon_r + \varepsilon_\theta$. (d) Color map of the intensity of the first three harmonics of the signal associated to the IR active mode (E_{1u}) while scanning the SNOM tip along the cyan dashed line shown in panel (a). (e) IR phonon frequency dependence of the 2$^{\rm nd}$ and 3$^{\rm rd}$ harmonic on the radial distance r. The black solid line is a fit to the data assuming a linear dependence of the phonon frequency on $\varepsilon_{\rm tot}$, provided by Eqs. (3) and (5) of the main text.

Analogous measurements were performed for a third bubble, whose AFM mage is shown in Fig. 1.3(a). In this case, the linescan was acquired along a radius to limit the map acquisition time. The corresponding color plot is given in panel (b). A similar analysis to that discussed for the previous two bubbles was performed also for this bubble. As summarized in panel (c), from the frequency dependence on r —and in turn on $\varepsilon_{\rm tot} = \varepsilon_r + \varepsilon_\theta$— we determined a strain-free frequency $\omega^0_{\rm 1u} = (1369.9 \pm 2.3)$ cm^{-1} and the shift rate $\Delta_{\rm 1u} = (29.4 \pm 1.8)$ cm^{-1}/%, resulting in a Grüneisen parameter (see Equation 5 of the main text) $\gamma_{\rm 1u} = 2.15 \pm 0.12$.

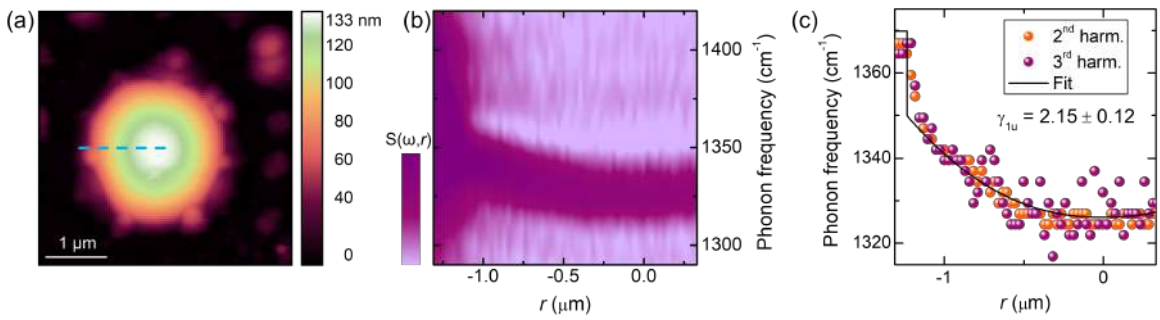

Figure 1.3: IR-active mode *vs* strain for a third bubble. (a) 2D AFM image of a circular hBN bubble, with $R = 1.23$ μm and $h_{\mathrm{m}} = 126$ nm ($h_{\mathrm{m}}/R = 0.102$) and created in an hydrogenated sample (beam energy equal to 34 eV). (b) Amplitude line scan of the 2nd harmonic signal associated to the IR active mode ($E_{1\mathrm{u}}$) along the cyan dashed line shown in panel (a). (c) IR phonon frequency dependence of the second and third harmonic line scans as a function of the radial distance r. The black solid line is a fit to the data assuming a linear dependence as extracted from the phonon frequency on $\varepsilon_{\mathrm{tot}}$, provided by Eqs. (3) and (5) of the main text.

Supporting Note 2. Raman mapping measurements in hBN bubbles

In this section, we show additional Raman mapping measurements taken along the diameter of other hydrogen- (or deuterium-) filled hBN bubbles. In panel (a) of Figs. 2.1 and 2.2, we show the false color plots of the intensity associated to the Raman spectra measured along the diameter of two different hBN bubbles. The most intense peak of the plots is assigned to the E_{2g} mode of the unstrained hBN bulk under the bubble. The weak peak that shifts as a function of the position of the excitation spot is the E_{2g} mode of the hBN layers comprised in the bubble. In panels (b), we show the corresponding Raman spectra, stacked by y-offset. Finally, in panels (c), we show the dependence of the Raman mode frequency as a function of the distance from the center r. We also show the fit to the experimental data to extract the Grüneisen parameter of the Raman mode.

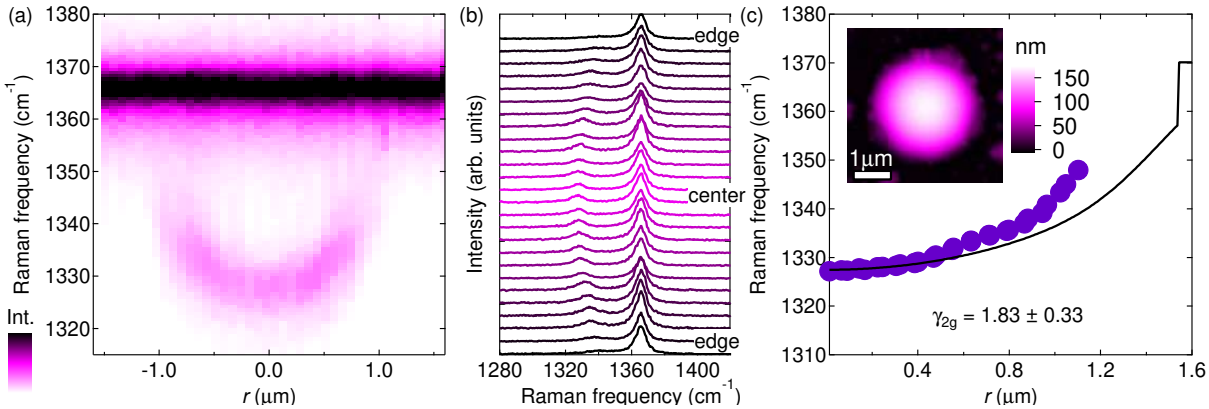

Figure 2.1: Summary of the Raman measurements performed on a hBN bubble with $R = 1.59$ μm and $h_m = 181$ nm ($h_m/R = 0.114$) and created in a deuterated sample (beam energy equal to 6 eV). (a) False color image of the intensity of Raman spectrum as a function of position along a diameter of a bubble. (b) Corresponding Raman spectra. (c) E_{2g} Raman mode frequencies as a function of the distance from the center of the bubble r. The solid line is a linear fit. The Grüneisen parameter is $\gamma_{2g} = 1.83 \pm 0.33$, which corresponds to a shift rate of $\Delta_{2g} = (25.1 \pm 4.5)$ cm^{-1}/%.

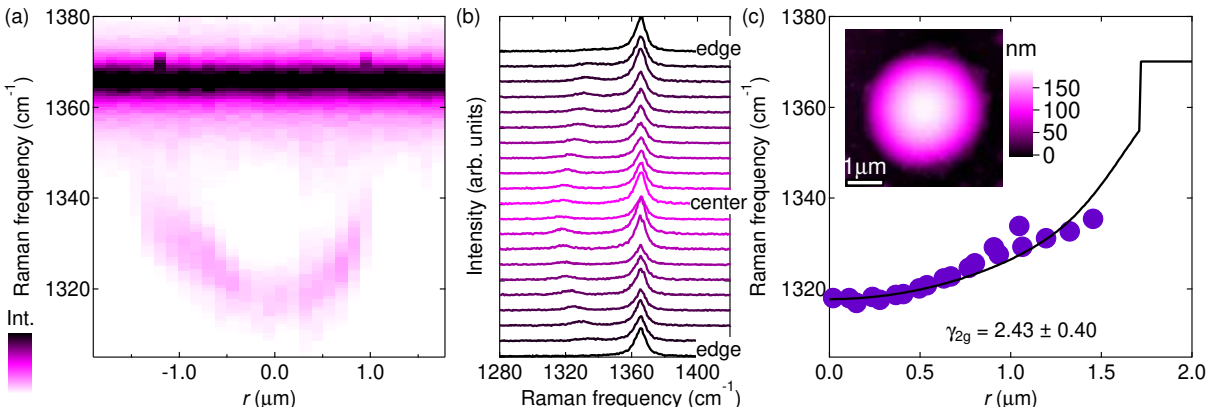

Figure 2.2: Summary of the Raman measurements performed on a hBN bubble with $R = 1.71$ μm and $h_m = 179$ nm ($h_m/R = 0.105$) and created in a deuterated sample (beam energy equal to 6 eV). (a) False color image of the intensity of Raman spectrum as a function of position along a diameter of a bubble. (b) Corresponding Raman spectra. (c) E_{2g} Raman mode frequencies as a function of the distance from the center of the bubble r. The solid line is a linear fit. The Grüneisen parameter found experimentally for this bubble is $\gamma_{2g} = 2.43 \pm 0.40$, which corresponds to a shift rate of $\Delta_{2g} = (33.2 \pm 5.2)$ cm^{-1}/%.

Supporting Note 3. Statistical analysis of the shift rates and Grüneisen parameters

To have a larger statistical analysis of the shift rates and Grüneisen parameters, we measured the Raman shifts at the center of about ten bubbles. We chose to perform Raman measurements rather than nano-FTIR measurements since the latter are more demanding. The resulting histogram is shown in Fig. 3.1. A Gaussian fit to the data provides an average shift with respect to the frequency of the unstrained membrane (assumed to be $\omega_{2g}^0 = 1370$ cm^{-1}) equal to 53 ± 11 cm^{-1}. To estimate the Grüneisen parameter, we need to estimate the average strain at the bubble center. Indeed, the latter is related to the aspect ratio via the following equation [2]:

$$\varepsilon^{\text{center}} = 0.715 \cdot \left(\frac{h_{\text{m}}}{R}\right)^2, \tag{3.3}$$

We thus considered the aspect ratios measured for a hundredth of bubbles (see Fig. 1(f) of the main text), and estimated a average value equal to 0.115 ± 0.011, see Fig. 3.1. In turn, from Eq. 3.3, we estimate $\varepsilon^{\text{center}} = (1.90 \pm 0.35)\%$. We can finally estimate the average Grüneisen parameter as:

$$\gamma_{2g} = \frac{\omega_{2g}^{\text{center}} - \omega_{2g}^0}{\omega_{2g}^0 \cdot \varepsilon^{\text{center}}}, \tag{3.4}$$

getting $\gamma_{2g} = 2.04 \pm 0.48$. This value agrees well with that estimated via Raman mapping measurements (see Fig. 3 of the main text and Supporting Note 2).

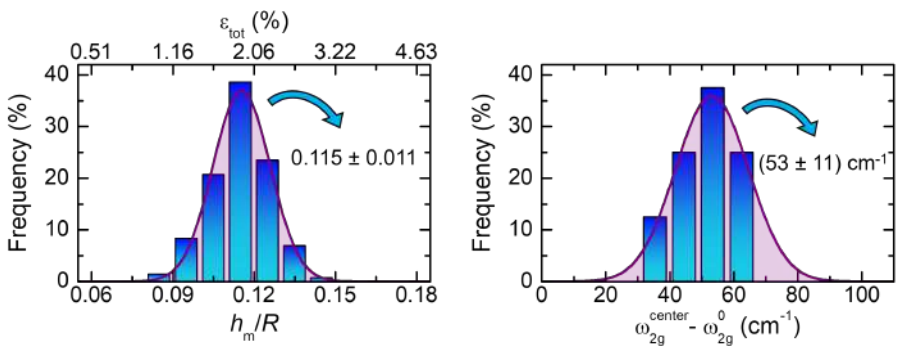

Figure 3.1: Histograms of the aspect ratios h_{m}/R (left) and Raman shifts measured at the summit of the bubbles $\omega_{2g}^{\text{center}} - \omega_{2g}^0$ (right). The Raman shift was calculated with respect to the unstrained value, which is assumed to be $\omega_{2g}^0 = 1370$ cm^{-1}. A Gaussian fit to the data (purple) provides the average values for both the two quantities.

Supporting Note 4. Polarization-resolved Raman measurements in hBN bubbles

Lineshape fitting of the polarization-resolved Raman measurements

To extract the intensity of the two Raman modes E_{2g}^{+} and E_{2g}^{-} as a function of the polarization angle of the Raman-scattered light ϕ, we performed a two-step analysis. We first fitted the spectra measured at different polarization angles with two Lorentzians (one for the Raman peak of the bubble, another for that of the unstrained bulk). This analysis allowed us to determine the maximum and minimum frequencies corresponding to the oscillating behavior observable in Fig. 5(a) of the main text. These maximum and minimum frequencies correspond to ω_{1u}^{+} and ω_{1u}^{-}, respectively. We then performed an additional fitting, using three Lorentzian functions, where we fixed the frequencies of the two Lorentzians used to fit the Raman peak of the bubble to the ω_{1u}^{+} and ω_{1u}^{-}. All the intensities shown in the main text and in the Supplementary Information are normalized to the intensity of the Raman peak of bulk hBN. E_{2g} modes of unstrained hBN are expected to show no dependence on the polarization of the scattered light [10], hence this normalization does not alter the polarization dependence of the $E_{2g}^{\pm}$ modes of the bubble.

In Fig. 4.1, we show the spectra measured at directions parallel ($\phi = 0°$) and perpendicular ($\phi = 90°$) with respect to the direction of the strain. The fitting of these two spectra demonstrate that the Raman peak measured on the bubble can be well reproduced with a single Lorentzian (the second Lorentzian with a negligible amplitude is also shown in Fig. 4.1). We show also the spectrum measured at an intermediate angle ($\phi = 135°$), in which the two Lorentzian curves the frequencies corresponding to the split Raman peaks have a comparable amplitude.

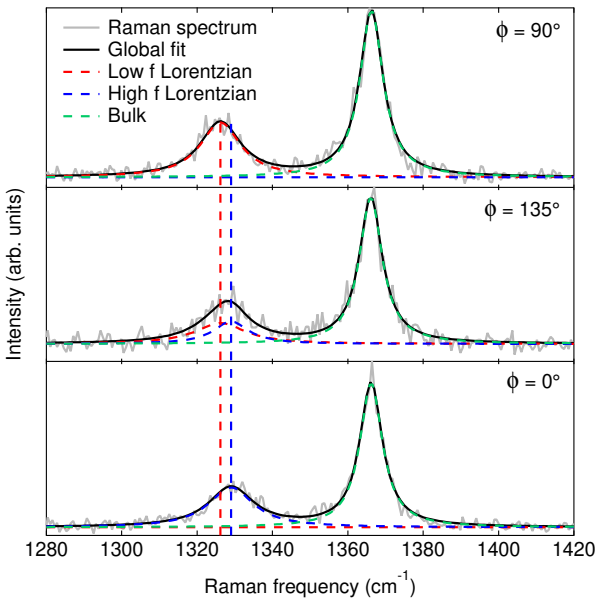

Figure 4.1: Raman spectra measured at three different polarization angles ϕ. In the bottom (top) panel, the spectrum measured at a polarization parallel (perpendicular) to the strain direction is shown. In the central panel, a spectrum measured at the intermediate angle is displayed.

Polarization measurements of another bubble

Analogous measurements to those shown in Fig. 5 of the main text were taken on a second bubble. The bubble has $R = 2.04$ μm and $h_{\mathrm{m}} = 216$ nm ($h_{\mathrm{m}}/R = 0.106$) and was created in a deuterated sample (beam energy equal to 25 eV). Fig. 4.2(a) shows an intensity map formed

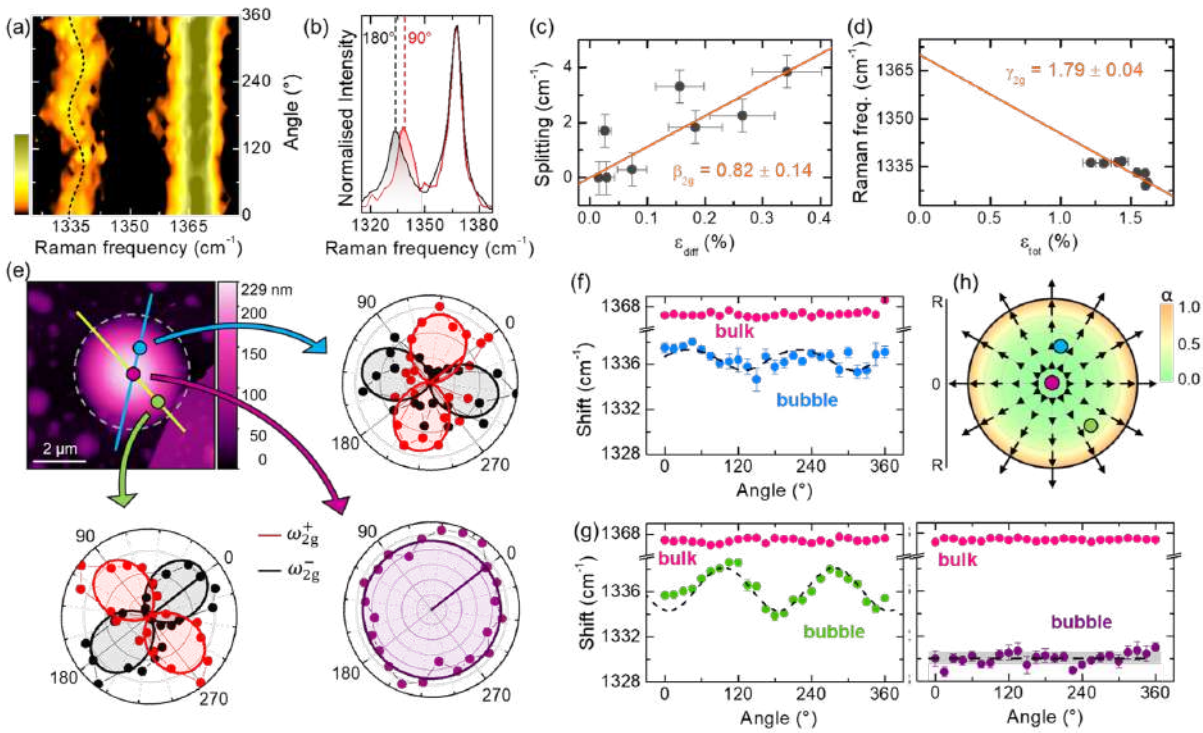

Figure 4.2: (a) Color map of the intensity of the E_{2g} Raman mode as a function of the angle of the polarization analyzer. The bulk mode at ∼1367 cm^{-1} shows no modulation. The dome mode at ∼1335 cm^{-1} shows a clear frequency oscillation, as highlighted by the black dashed line. (b) Two illustrative spectra corresponding to perpendicular angles equal to 90° and 180°. A splitting is clearly visible. (c-d) Summary of the splittings *vs* $\varepsilon_{\text{diff}}$ (c) and average frequencies *vs* ε_{tot} (d) measured by performing a similar analysis on several points over the bubble. The corresponding strain values were estimated via FEM calculations. The solid lines are linear fits. (e) AFM image of the studied hBN bubble. The measurements of panels (a-b) were acquired in the position highlighted by the green dot. Fitting procedures of the spectra allow us to derive the polar plot of the intensities of the low (black) and high (red) frequency Raman modes as a function of the analyzer angle. Analogous polar plots were derived from the measurements acquired on the purple and cyan dots. The solid lines in the polar plots are fits to the data. (f) Average frequency behavior obtained from the measurements acquired on the cyan dot. The dashed line follows the sinusoidal behavior of the frequency, which is caused by the strain anisotropy. (g) Average frequency behavior analogous to that of panel (f) but referring to the green and purple dots. (h) Spatial distribution of the strain anisotropy $\alpha = (\varepsilon_r - \varepsilon_\theta)/(\varepsilon_r + \varepsilon_\theta)$, determined based on FEM calculations. The arrows point to the direction of the strain field. Their length is calculated as $\log_{10}(100\alpha)$. The cyan, purple and green dots are in one-to-one correspondence with those superimposed to the AFM image of panel (e).

by polarization-dependent μ-Raman spectra recorded on a given point of the bubble. While the E_{2g} bulk mode at $\sim$ 1367 cm^{-1} remains constant in intensity and frequency, the strain-softened E_{2g} mode of the bubble at $\sim$ 1335 cm^{-1} exhibits a sinusoidal behavior of its center-of-mass frequency, pointing to a mode splitting. The splitting is clearly visible from the spectra of Fig. 4.2(b), recorded with opposite polarizations ($\phi = 180°$ and 90°, corresponding to a minimum and a maximum of the sinusoidal behavior, respectively). Similar measurements were taken on several other points of the bubble, in order to determine the splitting and average Raman frequency. From the knowledge of the radial distance r, it was possible to establish the radial and circumferential strain components corresponding to each set of data via FEM calculations. In panels (c) and (d), we display the measured splittings *vs* $\varepsilon_{\text{diff}}$ and the average frequencies *vs* ε_{tot}, respectively. From a linear fit, we could determine the shear deformation potential and Grüneisen parameter. From a detailed analysis of the polarization-resolved measurements, it is possible to determine also the angular dependence of the high-frequency and low-frequency modes. This is

exemplified in panel (e) for three different points of the bubble. The latter are highlighted by the colored dots superimposed to the AFM image of the bubble. It should be noticed that the data displayed in panels (a) and (b) were acquired on the green spot superimposed to the AFM image in panel (e). Indeed, the angular behavior follows the same rotation of the strain direction. To make it more apparent, the polar plots were rotated counter-clockwise by 38°. In such a manner, it is possible to notice how the red lobes (corresponding to the high-frequency mode) are always aligned parallel to the strain axes, indicated in cyan and green on the AFM image. At the bubble center (purple dot), instead, no splitting could be observed and the bubble mode remains constant in intensity when varying the angle of the polarization analyzer. Indeed, the existence of a splitting and in turn the presence of two oppositely-polarized modes is a consequence of the presence of an anisotropic strain. The extent of the anisotropy manifests itself in the amplitude of the oscillating behavior of the center of mass frequency. This is exemplified in panel (f) for the cyan point, where a splitting of 1.8 cm^{-1} was measured. Indeed, as shown in panel (g), an analysis of the center of mass frequency reveals a noticeably larger splitting for the green point —equal to 3.8 cm^{-1}— and the absence of splitting for the purple point. This is attributable to the fact the cyan point corresponds to an r value in between those of the purple point —where the anisotropy is null— and of the green point —where the anisotropy is larger— as highlighted by the anisotropy plot in panel (h).

Supporting Figure 1. Optical and AFM images of an H-irradiated flake

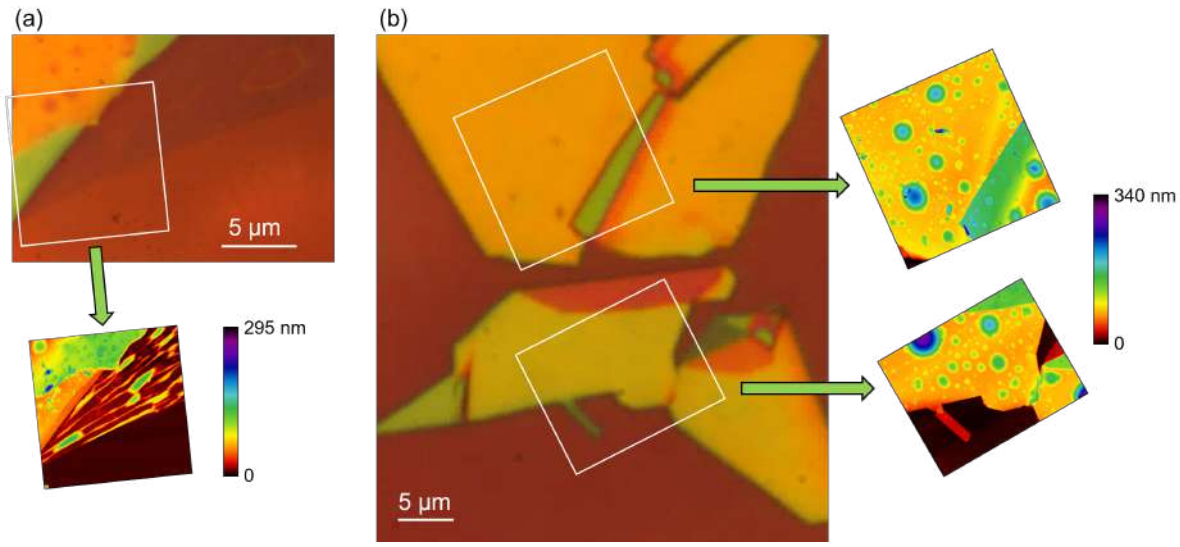

Figure S1. (a) Optical image of an H-irradiated hBN flake consisting of a thicker part on the left and a thinner part on the right. Elongated features can be barely seen in the thin part. AFM measurements confirm the presence of wrinkles and irregular structures. (b) Optical image of a thick H-irradiated hBN flake. Although optically the flake surface looks flat, AFM measurements reveal the presence of circular bubbles.

Supporting Figure 2. AFM characterization before and after H-irradiation

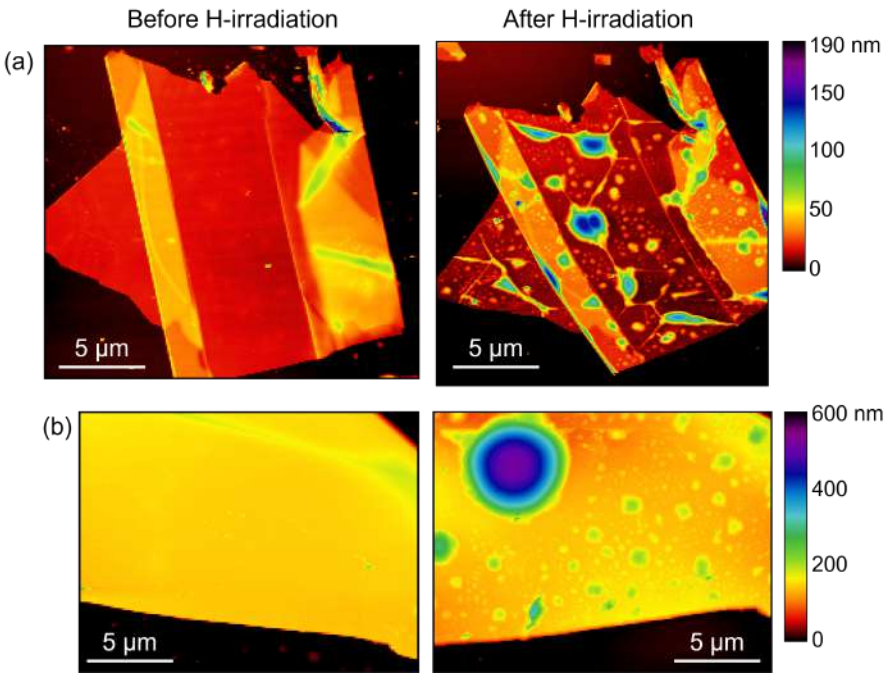

Figure S2. (a) AFM image of a hBN flake (thickness $t \approx 15$ nm) before and after H-irradiation. While prior to irradiation the flake surface looks flat, after the H-treatment bubbles, wrinkles and irregular structures are present on the flake. (b) Same for a thicker flake (thickness $t \approx 160$ nm). In this case, after the H-treatment only bubbles formed.

Supporting Figure 3. Bubbles and wrinkles in hBN

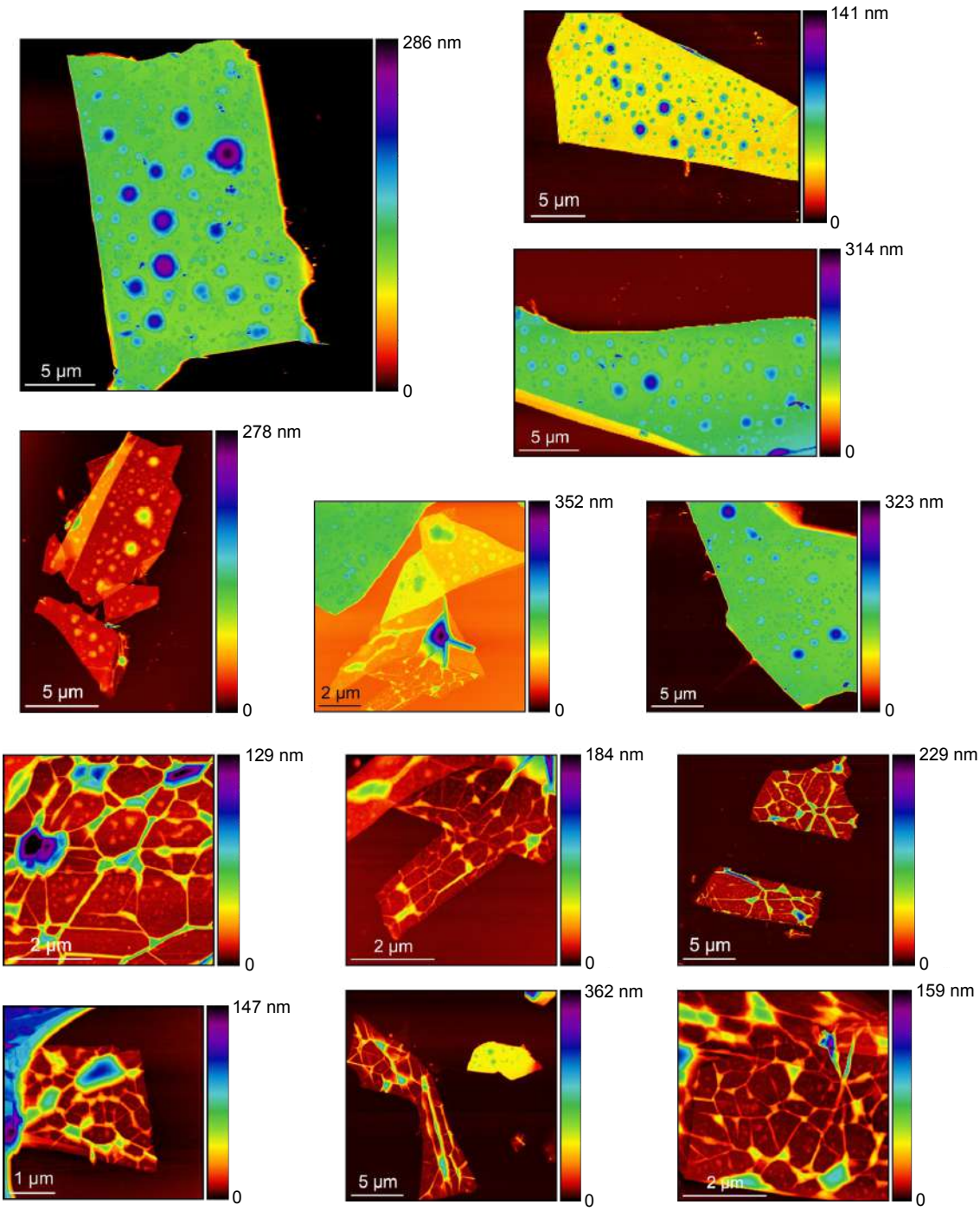

Figure S3. This figure shows AFM images of several hBN flakes following hydrogen- or deuterium- irradiation. As discussed in the main text, depending on the flake thickness either bubbles or wrinkles form.

The formation of wrinkles and irregular structures in the thinnest flakes ($t \lesssim 10\,\mathrm{nm}$) resembles the creation of irregularly shaped bubbles in graphene, achieved by high-energy ion-irradiation (500 keV) [11]. In that work, the density of observed features was much higher than the density of impinging ions (1×10^9 cm^{-2}), and the formation of these structures was thus attributed to an additional gas release from the SiO_2 substrate, with the gas remaining trapped

at the flake-substrate interface. The low beam energies used in our case rule out a significant gas release from the substrate [12]. However, here we employed ion doses 8 orders of magnitude larger than in Ref. [11], that justifies the formation of molecular hydrogen at the flake-substrate interface for $t \lesssim 10$ nm. The formed molecular hydrogen may accumulate and percolate, which originates irregular structures and wrinkles in the thinnest flakes (as shown in this figure and in Fig. 1(c) of the main text). On the other hand, the formation of spherically-shaped bubbles in thick flakes ($t \gtrsim 10$ nm) can be attributed to the formation of molecular hydrogen that remains trapped in the hBN interlayers, as observed in H plasma-treated hBN [13], and in TMD bubbles [14]. In this respect, one should consider that the bubbles form as a consequence of the energy balance between the gas expansion, the hBN membrane elastic energy and the adhesion energy between the hBN membrane and the parent flake beneath or the substrate [2]. The spherical shape of the bubbles derives from the minimization of the total energy of the system. Indeed, in between different crystal planes within a hBN flake, there is a perfect adhesion between the planes. This perfect adhesion guarantees that —when hydrogen molecules form— the gas expands isotropically, leading to the blistering of spherically-shaped bubbles. Instead, the SiO_2/hBN interface may be not as ideal due to a non-perfect adhesion between the flake and the substrate. This non-perfect adhesion can be caused by the deposition process itself, during which unavoidably present contaminants such as hydrocarbons or air are trapped, by the presence of debris, impurities or tape residuals, by the presence of steps in the deposited flake, by small strain transfers to the flake itself, etc. All these factors contribute to the creation of preferential directions along which the H_2 gas expands, giving rise to the formation of irregular structures and wrinkles.

Supporting Figure 4. Bubble thickness

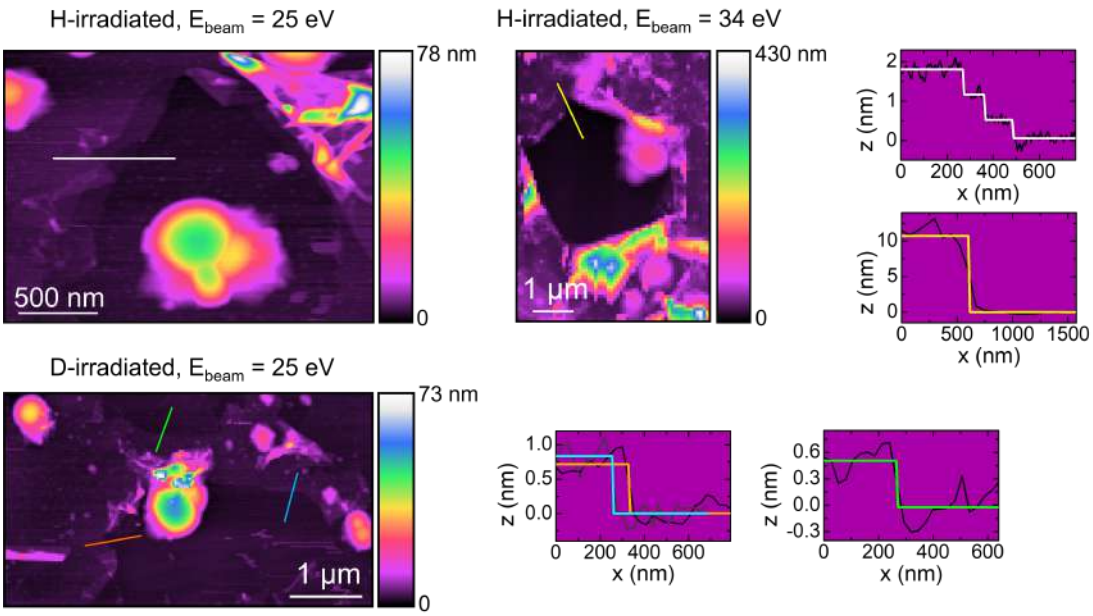

Figure S4. AFM images of three irradiated samples, after causing the explosion of some bubbles. The three samples were irradiated under different conditions, *i.e.* by using either hydrogen, H, or deuterium, D, ions and different beam energies.

In the sample irradiated with a 25-eV H-ion-beam (top left), the crater left by an exploded bubble can be seen. In one of the edges (white line) several steps can be noticed, suggesting that the bubble thickness was of several layers. By fitting the profile with a multiple step function (plot on the right), we estimate a total thickness of 1.8 nm. This crater is the shallowest one measured in hydrogenated samples. Interestingly, other bubbles are present within the crater, indicating how the exploded bubble possibly had a Russian-doll-like structure.

A crater can also be noticed in the sample irradiated with a 34-eV H-ion-beam (top center). In this case, it can be immediately noticed how the crater is deeper. A fit via a step function of the profile acquired along the yellow line points to a thickness of 10.7 nm. Other craters in hydrogenated samples featured thicknesses in between 2 and 12 nm.

Finally, in the sample deuterated with a 25-eV D-ion-beam, two craters can be noticed in the top part and bottom part of the image. One of the craters (bottom one) is relatively big, and by analysing two profiles — acquired along the orange and cyan lines — we estimated thicknesses of 0.71 nm (orange profile) and 0.83 nm (cyan one). The smaller crater in the top part of the image shows an ever smaller thickness of 0.52 nm, as estimated by an analysis of the profile acquired along the green line.

We measured several other profiles and our analysis suggest that in deuterated samples (beam energies between 6 eV and 25 eV) the bubbles are generally thinner than those formed in hydrogenated samples (beam energies between 6 eV and 34 eV).

Supporting Figure 5. Durability of hBN bubbles

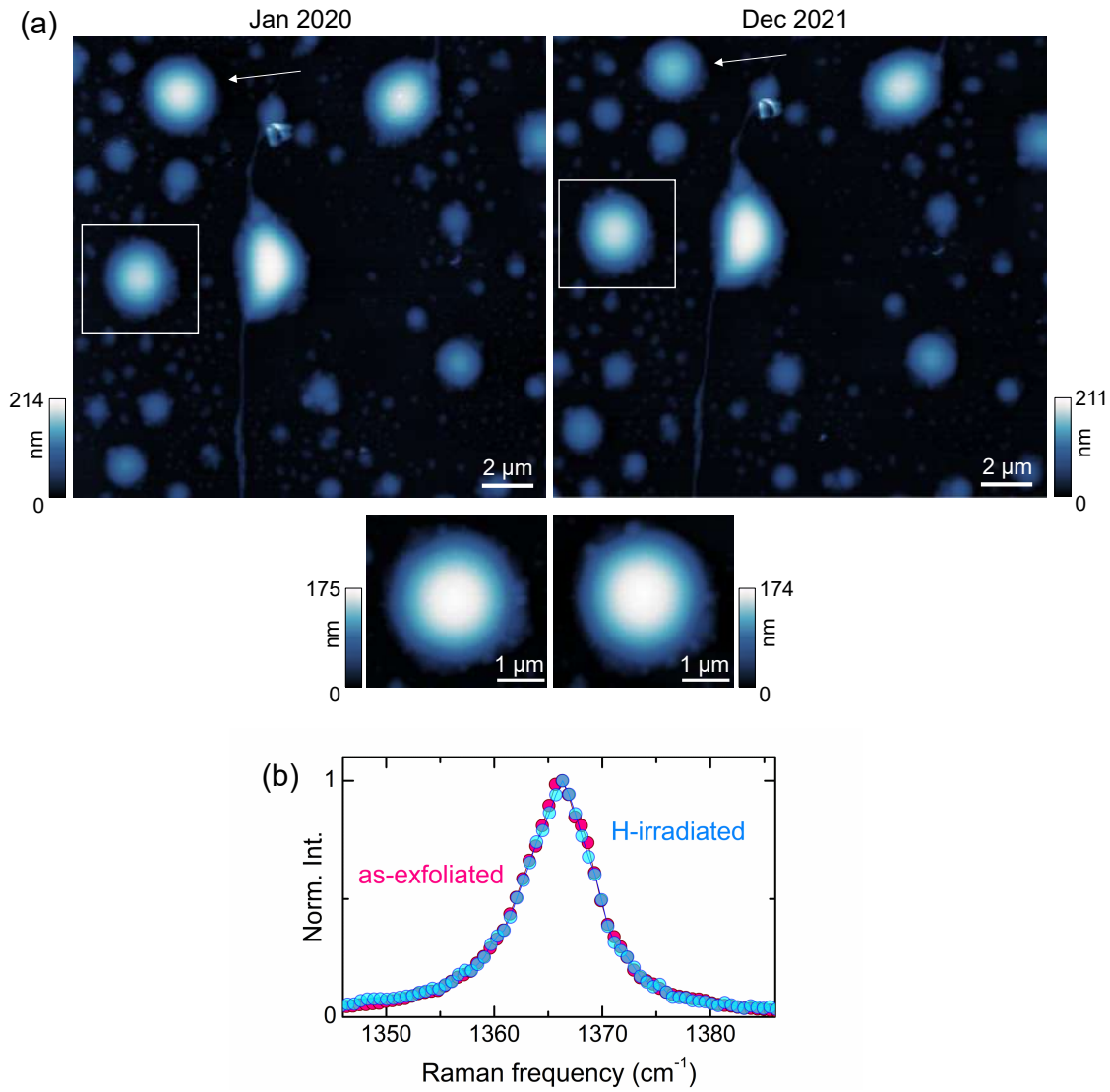

Figure S5. (a) Top panels: AFM images of an hBN flake irradiated with a 6-eV deuterium beam. The image on the right was recorded 23 months after that on the left, in about the same area. The white arrows indicate a bubble, which deflated over time. The other bubbles remained instead almost unchanged. In particular, the white squares highlight a bubble, whose higher resolution AFM images are displayed in the bottom panels. Bottom panels: Higher-resolution AFM images of a same bubble recorded after 23 months, showing that no sizable variations in the bubble size and shape occurred after about two years. (b) μ-Raman spectra of the E_{2g} hBN bulk mode recorded on an as-exfoliated (magenta dots) and H-irradiated (light blue dots). The latter was acquired on a flat area close to a bubble. No variation in the mode lineshape can be noticed after H irradiation.

Supporting Figure 6. AFM and FEM calculations of the bubble studied by Raman spectroscopy

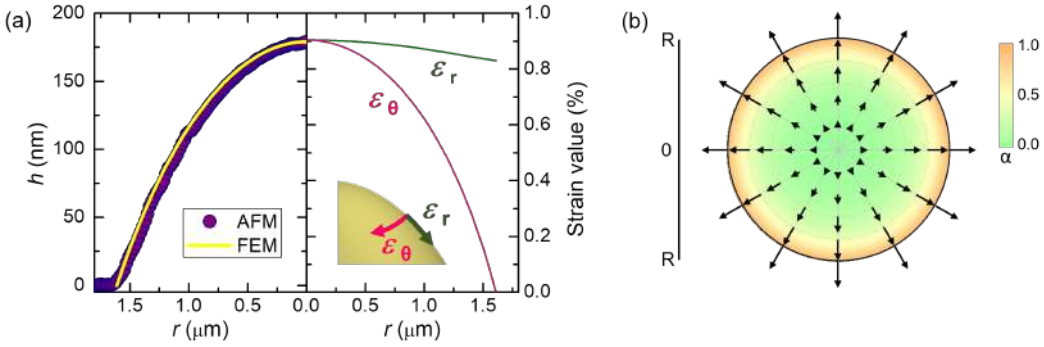

Figure S6. (a) Left: AFM profile (circles) along a radius of the bubble studied by Raman spectroscopy (see Figs. 4 and 5 of the main text). The yellow line is the height profile simulated via FEM numerical calculations. Right: Radial dependence —obtained by FEM calculations— of the in-plane circumferential (ε_θ) and radial (ε_r) strain components, a sketch of which is depicted as inset. (b) Spatial distribution of the strain anisotropy, defined as: $\alpha = (\varepsilon_r - \varepsilon_\theta)/(\varepsilon_r + \varepsilon_\theta)$. The arrows indicate the direction of the strain field —dictated by the radial strain component— and their length is proportional to $\log_{10}(100 \cdot \alpha)$.

References

[1] P. Wang, W. Gao, Z. Cao, K. M. Liechti, and R. Huang, *Numerical analysis of circular graphene bubbles*, J. Appl. Mech. **80**, 040905 (2013).

[2] E. Blundo, T. Yildirim, G. Pettinari, and A. Polimeni, *Experimental Adhesion Energy in van der Waals Crystals and Heterostructures from Atomically Thin Bubbles*, Phys. Rev. Lett. **127**, 4, 046101 (2021).

[3] F. Huth, A. Govyadinov, S. Amarie, W. Nuansing, F. Keilmann, and R. Hillenbrand, *Nano-FTIR absorption spectroscopy of molecular fingerprints at 20 nm spatial resolution*, Nano Lett. **12**, 8, 3973–3978 (2012).

[4] S. Mastel, A. A. Govyadinov, T. V. de Oliveira, I. Amenabar, and R. Hillenbrand, *Nanoscale-resolved chemical identification of thin organic films using infrared near-field spectroscopy and standard Fourier transform infrared references*, Appl. Phys. Lett. **106**, 2, 023113 (2015).

[5] Z. Shi, H. A. Bechtel, S. Berweger, Y. Sun, B. Zeng, C. Jin, H. Chang, M. C. Martin, M. B. Raschke, and F. Wang, *Amplitude- and phase-resolved nanospectral imaging of phonon polaritons in hexagonal boron nitride*, ACS Photonics **2**, 7, 790–796 (2015).

[6] P. Li, M. Lewin, A. V. Kretinin, J. D. Caldwell, K. S. Novoselov, T. Taniguchi, K. Watanabe, F. Gaussmann, and T. Taubner, *Hyperbolic phonon-polaritons in boron nitride for near-field optical imaging and focusing*, Nat. Commun. **6**, 1, 7507 (2015).

[7] P. Schmidt, F. Vialla, S. Latini, M. Massicotte, K.-J. Tielrooij, S. Mastel, G. Navickaite, M. Danovich, D. A. Ruiz-Tijerina, C. Yelgel, V. Fal'ko, K. S. Thygesen, R. Hillenbrand, and F. H. L. Koppens, *Nano-imaging of intersubband transitions in van der Waals quantum wells*, Nat. Nanotech. **13**, 1035 (2018).

[8] S. L. Moore, C. J. Ciccarino, D. Halbertal, L. J. McGilly, N. R. Finney, K. Yao, Y. Shao, G. Ni, A. Sternbach, E. J. Telford, B. S. Kim, S. E. Rossi, K. Watanabe, T. Taniguchi, A. N. Pasupathy, C. R. Dean, J. Hone, P. J. Schuck, P. Narang, and D. N. Basov, *Nanoscale lattice dynamics in hexagonal boron nitride moiré superlattices*, Nat. Commun. **12**, 5741 (2021).

[9] A. A. Govyadinov, S. Mastel, F. G. F, A. Chuvilin, P. S. Carney, and R. Hillenbrand, *Recovery of permittivity and depth from near-field data as a step toward infrared nanotomography*, ACS Nano **8**, 6911 (2014).

[10] Y. Wang, C. Cong, C. Qiu, and T. Yu, *Raman spectroscopy study of lattice vibration and crystallographic orientation of monolayer MoS_2 under uniaxial strain*, Small **9**, 17, 2857–2861 (2013).

[11] E. Stolyarova, D. Stolyarov, K. Bolotin, S. Ryu, L. Liu, K. T. Rim, M. Klima, M. Hybertsen, I. Pogorelsky, I. Pavlishin, K. Kusche, J. Hone, P. Kim, H. L. Stormer, V. Yakimenko, and G. Flynn, *Observation of graphene bubbles and effective mass transport under graphene films*, Nano Lett. **9**, 332 (2009).

[12] A.-M. Lanzillotto, T. E. Madey, and R. A. Baragiola, *Negative-ion desorption from insulators by electron excitation of core levels*, Phys. Rev. Lett. **67**, 2, 232 (1991).

[13] L. He, H. Wang, L. Chen, X. Wang, H. Xie, C. Jiang, C. Li, K. Elibol, J. Meyer, K. Watanabe, T. Taniguchi, Z. Wu, W. Wang, Z. Ni, X. Miao, C. Zhang, D. Zhang, H. Wang, and X. Xie, *Isolating hydrogen in hexagonal boron nitride bubbles by a plasma treatment*, Nat. Commun. **10**, 2851 (2019).

[14] D. Tedeschi, E. Blundo, M. Felici, G. Pettinari, B. Liu, T. Yildrim, E. Petroni, C. Zhang, Y. Zhu, S. Sennato, Y. Lu, and A. Polimeni, *Controlled Micro/Nanodome Formation in Proton-Irradiated Bulk Transition-Metal Dichalcogenides*, Adv. Mater. **31**, 1903795 (2019).